

REPORT



## A non-clinical comparative study of IL-23 antibodies in psoriasis

Li Zhou<sup>a</sup>, Yibing Wang<sup>b&</sup>, Qi Wan<sup>a</sup>, Fei Wu<sup>a</sup>, Jeffrey Barbon<sup>a</sup>, Robert Dunstan<sup>a</sup>, Stephen Gauld<sup>b</sup>, Mark Konrad<sup>a&</sup>, Laura Leys<sup>b</sup>, Richard McCarthy<sup>a</sup>, Marian Namovic<sup>b</sup>, Christine Nelson<sup>a</sup>, Gary Overmeyer<sup>a#</sup>, Denise Perron<sup>a&</sup>, Zhi Su<sup>b</sup>, Leyu Wang<sup>a</sup>, Susan Westmoreland<sup>a</sup>, Jun Zhang<sup>a&</sup>, Rui Zhu<sup>a</sup>, and Geertruida Veldman<sup>a</sup>

<sup>a</sup>Abbvie Bioresearch Center, Worcester; <sup>b</sup>Abbvie, North Chicago, USA

### ABSTRACT

Four antibodies that inhibit interleukin (IL)-23 are approved for the treatment of moderate-to-severe plaque psoriasis. Here, we present non-clinical data comparing ustekinumab, guselkumab, tildrakizumab and risankizumab with regard to thermostability, IL-23 binding affinity, inhibitory-binding mode, *in vitro* potency and *in vivo* efficacy. Risankizumab and guselkumab exhibited 5-fold higher affinity for IL-23 and showed more potent inhibition of IL-23 signaling than ustekinumab and tildrakizumab. Risankizumab and guselkumab completely blocked the binding of IL-23 to IL-23Ra as expected, whereas tildrakizumab did not. *In vitro*, risankizumab and guselkumab blocked the terminal differentiation of T<sub>H</sub>17 cells in a similar manner, while tildrakizumab had minimal impact on T<sub>H</sub>17 differentiation. In a human IL-23-induced ear-swelling mouse model, risankizumab and guselkumab were more effective than ustekinumab and tildrakizumab at reducing IL-17, IL-22, and keratinocyte gene expression. Our results indicate that the four clinically approved antibodies targeting IL-23 differ in affinity and binding epitope. These attributes contribute to differences in *in vitro* potency, receptor interaction inhibition mode and *in vivo* efficacy in preclinical studies as described in this report, and similarly may affect the clinical performance of these drugs.

### ARTICLE HISTORY

Received 10 February 2021  
Revised 27 July 2021  
Accepted 1 August 2021

### KEYWORDS

IL-23; IL-12; psoriasis; autoimmune disease; risankizumab; guselkumab; tildrakizumab; ustekinumab

### Introduction

Psoriasis is one of the most common autoinflammatory diseases and affects more than 125 million people worldwide.<sup>1</sup> This chronic immune-mediated condition is characterized by inflammatory skin lesions with hyperplasia of keratinocytes in the epidermis and infiltration of leukocytes, especially T cells into the dermis.<sup>2</sup> The initiation of disease pathogenesis involves the activation of dermal dendritic cells to secrete factors that support the differentiation of T helper 17 (T<sub>H</sub>17) cells.<sup>3</sup> One of these factors, the cytokine interleukin (IL)-23, is thought to be required for the maintenance and generation of pathogenic T<sub>H</sub>17 cells that produce the inflammatory cytokines IL-17 and IL-22, which in turn stimulate keratinocyte responses including proliferation and secretion of psoriasis associated mediators. Blocking the activity of IL-23 with neutralizing antibodies therefore offers an attractive therapeutic intervention for psoriasis.<sup>4</sup>

Four antibodies that inhibit IL-23 through interaction with either the p19 or p40 subunit have been approved by the U.S. Food and Drug Administration for the treatment of moderate-to-severe plaque psoriasis in adults. Ustekinumab, approved in 2009 and previously known as CNTO 1275, was generated using Medarex's transgenic HuMab-Mouse. It is a human IgG1, k monoclonal antibody that binds to the p40 subunit of IL-12 and IL-23.<sup>5,6</sup> Guselkumab, approved in 2017 and previously known as CNTO 1959, is a human IgG1, λ antibody

derived from the MorphoSys HuCAL phage display antibody library. It binds to the p19 subunit of IL-23 and inhibits the binding to the IL-23Ra receptor subunit.<sup>7</sup> Tildrakizumab, approved in 2018 and also known as MK-3222, is a humanized IgG1, k monoclonal antibody that is specific for the p19 subunit of IL-23.<sup>8</sup> Risankizumab, approved in 2019 and described as BI 655066, is a high-affinity antibody that binds to the p19 subunit and blocks its interaction with IL-23Ra receptor subunit.<sup>9</sup> It is a humanized IgG1, k antibody with L234A, L235A mutations to reduce unnecessary and unwanted FcγR interactions.

The p19 antibodies showed superiority against several standard-of-care biologics in clinical studies, as described for guselkumab versus anti-tumor necrosis factor (TNF) adalimumab,<sup>10–12</sup> tildrakizumab versus anti-TNF etanercept,<sup>13</sup> and risankizumab versus ustekinumab<sup>14–16</sup> and adalimumab.<sup>17</sup> The reported Psoriasis Area and Severity Index (PASI) 90 responses after long-term treatment are 43–62% for ustekinumab,<sup>18–20</sup> 76% for guselkumab,<sup>11,21</sup> 52–59% for tildrakizumab,<sup>13</sup> and 81% for risankizumab.<sup>15</sup> In addition to nonclinical attributes, such as affinity, potency and epitope, the clinical response rates are also driven by a variety of factors, including dose, dosing frequency, and serum half-life of the drug (Table 1).<sup>22–24</sup>

In this study, we compared ustekinumab, guselkumab, tildrakizumab and risankizumab in relevant assays used in a preclinical setting. The results from thermostability studies, target-binding studies, cellular potency assays, a T<sub>H</sub>17

**CONTACT** Li Zhou  [li.zhou@abbvie.com](mailto:li.zhou@abbvie.com)  Abbvie Bioresearch Center, 100 Research Drive, Worcester, MA 01605, USA

<sup>&</sup>Former Abbvie employee

<sup>#</sup>Retired Abbvie employee

 Supplemental data for this article can be accessed on the [publisher's website](#).

© 2021 Taylor & Francis Group, LLC

This is an Open Access article distributed under the terms of the Creative Commons Attribution-NonCommercial License (<http://creativecommons.org/licenses/by-nc/4.0/>), which permits unrestricted non-commercial use, distribution, and reproduction in any medium, provided the original work is properly cited.

**Table 1.** Biochemical, biophysical, and clinical parameters of the IL-23 antibodies.

Name	Target	Antibody format	Maintenance dosing regimen after 2 doses at Wk 0 and Wk 4	PASI 90 Week 28–52	Serum half-life (days)	T <sub>onset-DSC</sub> (°C)	T <sub>Agg</sub> (°C)
Ustekinumab	p40	hlgG1,k	45 or 90 mg Q12 Wk	43–62	15–45 <sup>A</sup>	56.7	70.3
Guselkumab	p19	hlgG1,λ	100 mg Q8 Wk	76	15–18 <sup>A,22</sup>	60.2	70.4
Tildrakizumab	p19	hlgG1,k	100 mg Q12 Wk	52–59	23 <sup>A,23</sup>	61.4	70.3
Risankizumab	p19	hlgG1 LALA,k	150 mg Q12 Wk	81	28 <sup>A,24</sup>	66.0	83.9

A. Serum half-life from approved labels.

T<sub>onset-DSC</sub> is the onset temperature of protein unfolding measured by DSC. T<sub>Agg</sub> is the onset temperature of protein aggregation measured by nanoDSF.

**Table 2.** Binding affinity and kinetics of IL-23 antibodies measured by SPR.

	Sc huIL-23 (n = 5)			Heterodimer huIL-23 (n = 3)		
	k <sub>a</sub> × 10 <sup>6</sup> (M <sup>-1</sup> s <sup>-1</sup> )	k <sub>d</sub> × 10 <sup>-5</sup> (s <sup>-1</sup> )	K <sub>D</sub> (pM)	k <sub>a</sub> × 10 <sup>5</sup> (M <sup>-1</sup> s <sup>-1</sup> )	k <sub>d</sub> × 10 <sup>-5</sup> (s <sup>-1</sup> )	K <sub>D</sub> (pM)
Risankizumab	1.0 ± 0.3	1.8 ± 1.0	21 ± 16	5.6 ± 0.6	2.3 ± 0.2	43 ± 7
Guselkumab	1.0 ± 0.4	2.6 ± 1.1	35 ± 27	4.7 ± 0.4	3.6 ± 0.3	77 ± 11
Tildrakizumab	1.2 ± 0.3	14.4 ± 7.3	136 ± 91	9.3 ± 0.6	21.1 ± 1.4	228 ± 6
Ustekinumab	2.1 ± 0.6	17.2 ± 11.7	106 ± 98	13.4 ± 2.0	30.8 ± 1.2	232 ± 23

Average values and standard deviations for k<sub>a</sub>, k<sub>d</sub>, K<sub>D</sub> were calculated from five (scIL-23) or three (heterodimeric IL-23) experiments, respectively. Measurements were done at 37°C in HBS-EP+ running buffer. .

differentiation assay and a human IL-23-induced ear-swelling mouse model shed light on the molecular attributes that may contribute to these antibodies' clinical efficacy.

## Results

### Antibody stability and potential deamidation sites

The conformational and colloidal stabilities of ustekinumab, guselkumab, tildrakizumab and risankizumab were assessed using differential scanning calorimetry (DSC) and nano differential scanning fluorimetry (nanoDSF) (Table 1, Supplemental Figure S1). All four antibodies displayed high onset temperatures of unfolding

(T<sub>onset-DSC</sub> > 56°C), suggesting they have good conformational stability, as well as high onset temperatures of protein aggregation T<sub>Agg</sub> (>70°C) as measured by nanoDSF, indicating good colloidal stability. Among these four antibodies, risankizumab has the highest

T<sub>onset-DSC</sub> (66.0°C) and T<sub>Agg</sub> (83.9°C). Guselkumab contains several potential deamidation sites in complementarity-determining region 2 of the heavy and light chains. However, prolonged *in vitro* incubation at pH 8.0 and pH 9.5 followed by liquid chromatography-mass spectrometry (LC-MS) analysis indicated that these residues were not prone to deamidation, as less than 15% deamidation was observed (Supplemental Table S1).

### Antibody interactions with IL-23 and Fc receptors

A central mechanism of therapeutic anti-IL-23 antibodies is the neutralization of free IL-23. The binding affinity for IL-23 may therefore be a major determinant of clinical efficacy. To assess the binding kinetics of the antibodies to human IL-23, we performed surface plasmon resonance (SPR) measurements at 37°C. The antibodies were captured on the chip surface using a goat anti-human IgG Fc polyclonal antibody. Different concentrations of the analyte, either single-chain (sc) or heterodimeric human IL-23, were interacted in consecutive cycles with surface-displayed IL-23 antibodies. The individual association

(k<sub>a</sub>) and dissociation (k<sub>d</sub>) rate constants and the equilibrium dissociation constant (K<sub>D</sub>) were calculated using global fitting to a 1:1 binding model. Risankizumab and guselkumab exhibited high affinity to human scIL-23 with mean K<sub>D</sub>s of 21 pM and 35 pM, respectively, whereas tildrakizumab and ustekinumab showed about a 5-fold lower affinity for scIL-23 than risankizumab with mean K<sub>D</sub>s of 136 pM for tildrakizumab and 106 pM for ustekinumab (Table 2 and Supplemental Figure S2). The affinities of the antibodies for heterodimeric IL-23 were slightly lower than for scIL-23 but followed a similar trend. The difference in K<sub>D</sub> between risankizumab and tildrakizumab/ustekinumab is mainly driven by risankizumab having an 8- to 13-fold slower dissociation rate constant (k<sub>d</sub>), indicating that risankizumab forms a more stable immune complex with IL-23.

Guselkumab, tildrakizumab and ustekinumab, which are human IgG1 with intact Fc, exhibited high monomeric binding to high-affinity FcγRs and low monomeric binding to low-affinity FcγRs, while risankizumab, which possesses the L234A, L235A mutations,<sup>9</sup> displayed the expected reduced binding to human FcγRI and FcγRIIIA V176 and undetectable binding to low-affinity FcγRs (data not shown). These Fc differences are not expected to result in a different biological outcome because FcγR-mediated effector function is not thought to be part of the mechanism of action of the IL-23 antibodies, as they bind a soluble cytokine and do not form multimeric antibody/antigen complexes.

Antibody interactions with the neonatal Fc receptor (FcRn) in the low pH environment of the endosome and subsequent dissociation at the neutral pH on the cell surface after recycling play a critical role in maintaining the long serum half-life of IgGs.<sup>25</sup> All IL-23 antibodies showed similar binding affinities of about 5 μM to FcRn at pH 6.0 and little binding at pH 7.4 in an SPR assay (data not shown). However, when antibodies were bound to an FcRn column and subjected to a pH gradient, guselkumab showed a delayed elution at physiological pH. In contrast, ustekinumab, tildrakizumab and risankizumab immediately eluted when the pH reached 7.4 (Supplemental Figure S3). Guselkumab's slower dissociation from FcRn may contribute to its shorter half-life in psoriasis patients (Table 1).

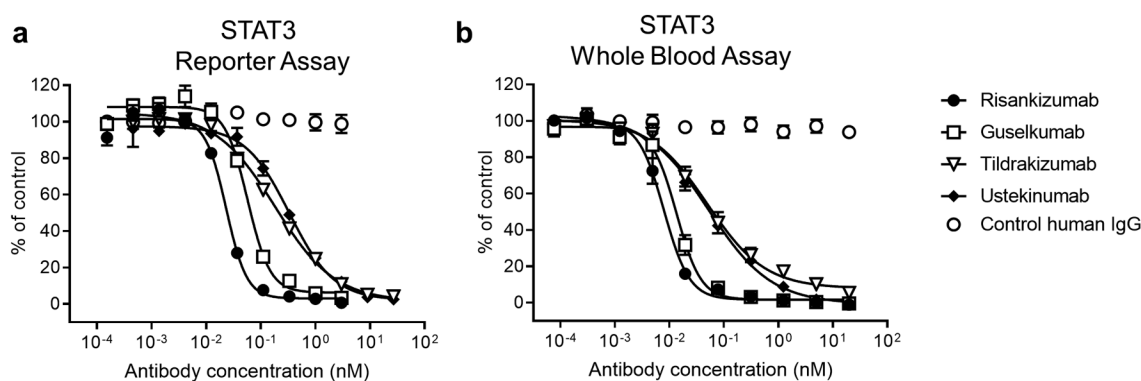


**Figure 1.** In vitro potency of the IL-23 antibodies. (a) Dose-dependent inhibition of STAT3 luciferase reporter expression in HeLa cells with the stimulation of 1 ng/mL IL-23 ( $n = 3$ ). (b) Dose-dependent inhibition of pSTAT3 expression by FACS in CD45<sup>+</sup> CD161<sup>hi</sup> cells from human whole blood with the stimulation of 1 ng/mL IL-23 ( $n = 6$  with 3 healthy donors). Data are plotted as mean  $\pm$  SEM. Antibody potency was determined by calculating the inhibitory concentration that results in 50% inhibition ( $IC_{50}$ ) and 80% inhibition ( $IC_{80}$ ) with 95% confidence interval (CI). Data and statistical analysis are summarized in (Table 3).

**Table 3.** In vitro cellular potency of IL-23 antibodies.

	STAT3 Reporter				pSTAT3 Whole Blood			
	$IC_{50}$ (pM)	95% CI	$IC_{80}$ (pM)	95% CI	$IC_{50}$ (pM)	95% CI	$IC_{80}$ (pM)	95% CI
Risankizumab	23	18–29	42	32–56	6	2–21	12	4–35
Guselkumab	59*	46–76	117**	89–155	10	3–34	20	7–55
Tildrakizumab	203***	157–262	1155***	873–1529	39**	12–129	197***	70–548
Ustekinumab	316***	244–408	1460***	1103–1933	40**	12–133	246***	88–692

Antibody potency was determined by calculating the inhibitory concentration that results in 50% inhibition  $IC_{50}$  and 80% inhibition  $IC_{80}$  with 95% confidence interval (CI). Pairwise comparison with risankizumab: \*  $p \leq 0.05$ , \*\*  $p \leq 0.001$ , \*\*\*  $p \leq 0.0001$ .

### Antibody activity in cell-based bioassays

The *in vitro* potency of the antibodies was compared in two different bioassays. The first, a STAT3-driven luciferase reporter assay, used HeLa cells recombinantly expressing the human IL-23R $\alpha$  and IL-12R $\beta$ 1 receptors (Figure 1a). Risankizumab inhibited IL-23-induced STAT3 signaling with an  $IC_{50}$  of 23 pM. Risankizumab was 2.6-fold more potent than guselkumab ( $p \leq 0.05$ ), 9-fold more potent than tildrakizumab ( $p \leq 0.0001$ ) and 14-fold more potent than ustekinumab ( $p \leq 0.0001$ ) based on calculated  $IC_{50}$ s of 59 pM, 203 pM and 316 pM, respectively (Table 3). The second pSTAT3 assay used human whole blood from healthy donors and measured increased pSTAT3 in CD45<sup>+</sup> CD161<sup>hi</sup> cells, which are IL-17 producing CD4<sup>+</sup>T<sub>H</sub> 17<sup>26</sup> and CD8<sup>+</sup> T<sub>C</sub>17 cells.<sup>27</sup> Upon stimulation with IL-23, risankizumab and guselkumab demonstrated similar potency with  $IC_{50}$  of 6 pM and 10 pM, respectively, whereas tildrakizumab and ustekinumab were about 6-fold less potent than risankizumab with  $IC_{50}$ s of 39 pM and 40 pM ( $p \leq 0.001$ )

(Figure 1b). A comparison of the  $IC_{80}$  values showed a similar trend, but with a greater potency differential. While risankizumab and guselkumab were able to achieve 80% inhibition in these assays at concentrations that were twice as high as their  $IC_{50}$  concentration, tildrakizumab and ustekinumab required significantly higher antibody concentrations to achieve 80% inhibition. As a result, risankizumab was able to achieve 80% inhibition at concentrations that were 16- to 35-fold lower than those required for tildrakizumab and ustekinumab as based on the calculated  $IC_{80}$  values (Table 3).

### Antibody epitope mapping

The antibody epitopes on IL-23 were compared (Figure 2). Ustekinumab's epitope is on the p40 subunit of IL-23,<sup>30</sup> while guselkumab, tildrakizumab and risankizumab all recognize the p19 subunit, albeit at slightly different epitopes. Tildrakizumab's epitope has been determined by x-ray crystallography in which K39, T42, W45, S46, P49, E101, S114-D118,

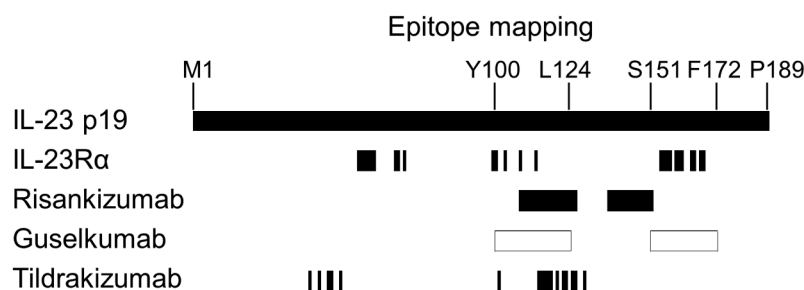


**Figure 2.** Epitope alignment of IL-23 R $\alpha$  and IL-23 antibodies on the IL-23p19 sequence. The epitopes of guselkumab (white boxes) and risankizumab (black boxes)<sup>9</sup> as determined by HDX-MS. The epitopes of tildrakizumab<sup>28</sup> and IL-23 R $\alpha$ <sup>29</sup> as determined by x-ray crystallography are shown in black bars.

P120, G122, Q123, H125, A126, L129 were identified as important contact residues within 4 Å of antigen.<sup>28</sup> Risankizumab's epitope has been determined by hydrogen deuterium exchange mass spectrometry (HDX-MS) to encompass I108-A126 and P137-S151.<sup>9</sup> Guselkumab's epitope, which was determined by HDX-MS in this study, involves residues in two peptide regions, Y100-L124 and S151-F172 (Supplemental Figure S4).

The binding interface of IL-23R $\alpha$  and IL-23 has been reported.<sup>29</sup> Both risankizumab and guselkumab showed overlapping epitopes with IL-23R $\alpha$  (Figure 2). Specifically, I108 and P113 are residues on IL-23 covered by risankizumab, guselkumab and IL-23R $\alpha$ . Residues Y100, L103, Q154-Q157, L159-L161, K164-K165, R167-S168 are additionally shared between guselkumab and IL-23R $\alpha$ . Interestingly, tildrakizumab and IL-23R $\alpha$  do not share critical contact residues on IL-23, despite tildrakizumab showing inhibitory activity in cellular potency assays.

### IL-23 receptor activation and antibody inhibitory binding mode characterization

IL-23 receptor activation requires assembly of the ternary complex consisting of IL-23R $\alpha$ , IL-23 and IL-12R $\beta$ 1. The IL-23p19 subunit is known to interact with IL-23R $\alpha$ , and the IL-23p40 subunit interacts with IL-12R $\beta$ 1.<sup>29</sup> Binding affinities of these two interacting pairs were measured by SPR to be 0.8 nM for the IL-23/IL-23R $\alpha$  and 19 nM for the IL-23/IL-12R $\beta$ 1 pair (Supplemental Figure S5). To further characterize the cytokine/receptor interaction, we also measured the dissociation constants of the ternary complex assembly. The binding affinity of IL-12R $\beta$ 1 for IL-23R $\alpha$ -bound scIL-23 was determined by SPR to be 56 nM, while IL-23R $\alpha$ 's affinity for IL-12R $\beta$ 1-bound scIL-23 was 6 nM (Supplemental Figure S5).

To investigate whether antibody-bound IL-23 would be blocked from binding to its receptors, we conducted binding studies using both recombinant IL-23 receptor proteins and IL-23 receptor expressing HEK293 cells.

The binding of antibody/IL-23 complexes to immobilized IL-23R $\alpha$  or IL-12R $\beta$ 1 was assessed by SPR. IL-23 pre-incubated with a saturating amount of ustekinumab or a control human

IgG1 antibody showed binding to IL-23R $\alpha$  as expected since ustekinumab bound to the p40 subunit would not interfere with the p19/IL-23R $\alpha$  interaction. IL-23/risankizumab and IL-23/guselkumab complexes did not show any binding to IL-23R $\alpha$ , indicating both risankizumab and guselkumab completely blocked the binding of IL-23 to IL-23R $\alpha$  (Figure 3a). Our result is consistent with previously reported data for these antibodies.<sup>7,9</sup> Surprisingly, the IL-23/tildrakizumab complex was still able to bind IL-23R $\alpha$ , even in the presence of a saturating amount of tildrakizumab. To better understand the inhibitory effect of tildrakizumab on the IL-23/IL-23R $\alpha$  interaction, the affinity of IL-23 for IL-23R $\alpha$  was determined in the presence and absence of a saturating amount of tildrakizumab. The presence of tildrakizumab reduced IL-23's affinity for IL-23R $\alpha$  by approximately 200-fold from 0.8 nM to 190 nM (Supplemental Figure S5), suggesting that tildrakizumab may inhibit the p19/IL-23R $\alpha$  interaction through a negative allosteric modulation rather than a competitive inhibition. Additionally, we investigated whether antibodies would bind to IL-23R $\alpha$ -bound IL-23. Consistently, risankizumab and guselkumab did not show binding to the IL-23R $\alpha$ -bound cytokine, while tildrakizumab and ustekinumab showed binding (Supplemental Figure S6). The binding of antibody/IL-23 complexes to immobilized IL-12R $\beta$ 1 was similarly assessed by SPR. IL-23 complexes with guselkumab, tildrakizumab and, to a lesser extent, risankizumab were able to bind to IL-12R $\beta$ 1 (Figure 3a). The IL-23/ustekinumab complex did not bind since ustekinumab is a competitive inhibitor of IL-23p40/IL-12R $\beta$ 1 binding.<sup>5,6,30</sup>

The binding of IL-23/antibody complexes to HEK293 cell lines expressing either one or both IL-23 receptor subunits was further assessed by fluorescence-activated cell sorting (FACS) (Figure 3b). IL-23/antibody complexes comprising Zenon-labeled antibody (10 nM) and human scIL-23 at concentrations ranging from 1.25 to 20 nM were added to cells for 1 hour on ice prior to FACS analysis. As expected, IL-23 in complex with ustekinumab showed strong binding to cells expressing IL-23R $\alpha$ , whereas IL-23 in complex with risankizumab or guselkumab did not. Under this experimental condition, IL-23/

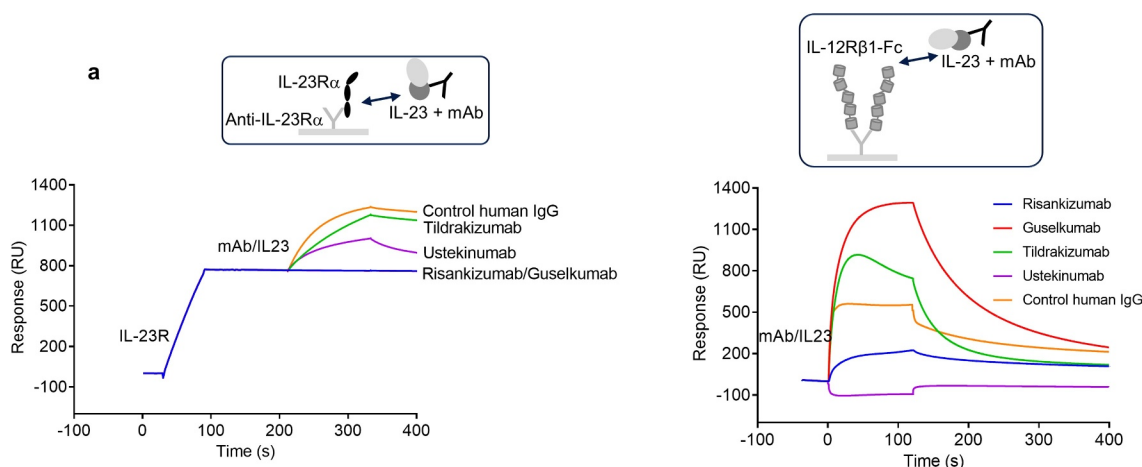


**Figure 3.** The binding mode of antibodies, IL-23 and IL-23 receptors characterized by SPR and FACS. (a) the SPR sensorgram of antibody/IL-23 complexes binding to IL-23R $\alpha$  (left) or IL-12R $\beta$ 1-Fc (right) immobilized on the chip. (b) IL-23/antibody complexes, comprising Zenon-labeled antibody (10 nM) and human scIL-23 at concentrations ranging from 1.25 to 20 nM, were added to HEK293 cells expressing either one or two IL-23 receptor subunits for one hour on ice prior to FACS analysis.

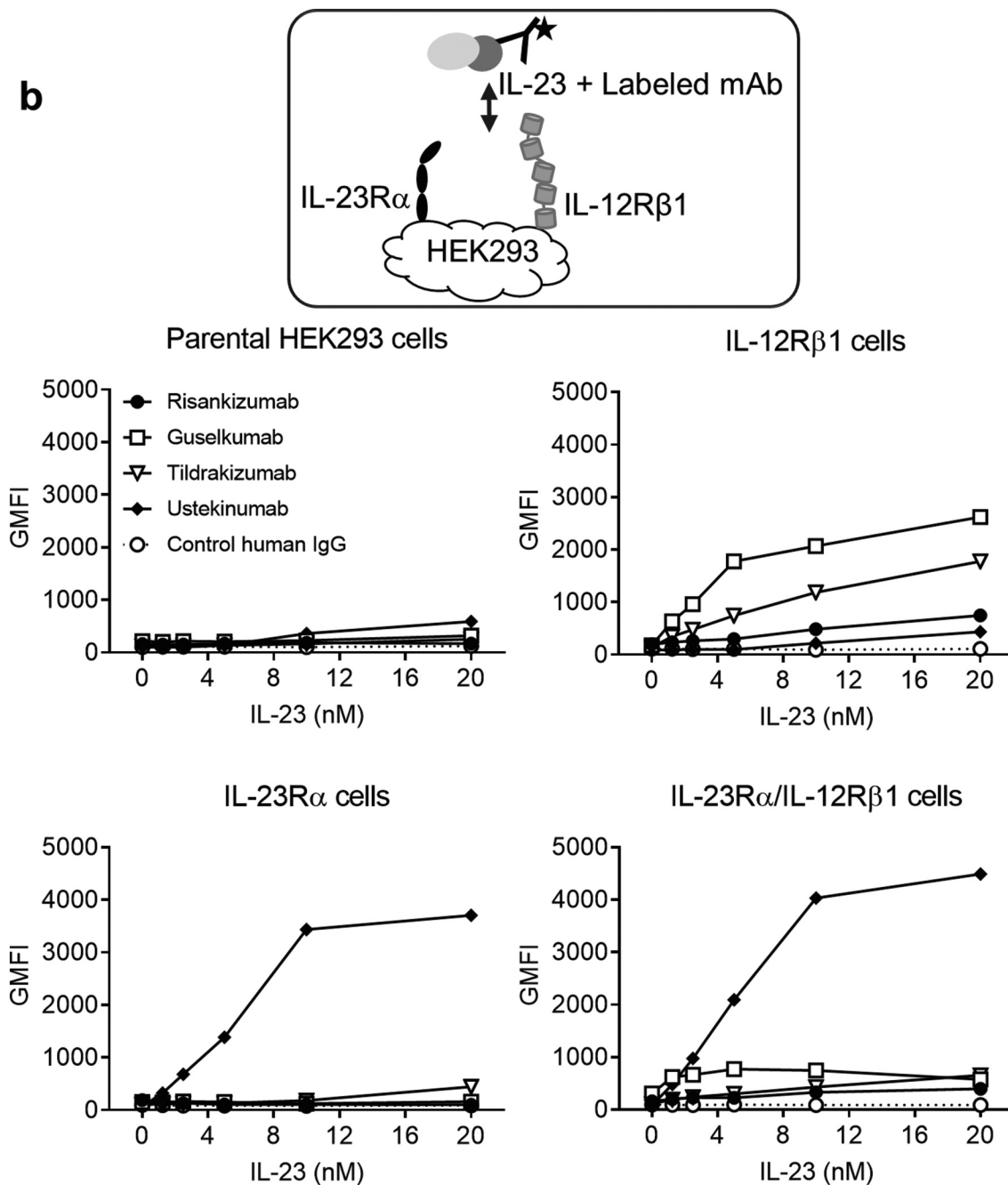


Figure 3. Continued.

tildrakizumab did not show observable binding to cells expressing IL-23R $\alpha$ . IL-23 precomplexed with the labeled anti-p19 antibodies showed binding to cells expressing IL-12R $\beta$ 1 to a different extent. These differences were not due to a difference in antibody labeling efficiency (data not shown). IL-23/guselkumab binding was strong, IL-23/tildrakizumab intermediate and IL-23/risankizumab binding was very low, suggesting that risankizumab's binding to the p19 subunit may create a steric hindrance or conformational change between the p40 subunit and IL-12R $\beta$ 1. Similar binding patterns were observed when IL-23 was first allowed to bind to cells expressing the individual receptors and bound IL-23 was detected using the labeled antibodies (Supplemental Figure S7).

#### ***T<sub>H</sub>17* differentiation**

We used an *in vitro* human T<sub>H</sub>17 differentiation assay to understand how IL-23 antibodies may affect the differentiation of naïve CD4<sup>+</sup> T (T<sub>naïve</sub>) cells toward T<sub>H</sub>17 cells. In this assay, T<sub>naïve</sub> cells were isolated from cord blood, activated with anti-CD3- and anti-CD28-coated beads and polarized into T<sub>H</sub>17 cells with a T<sub>H</sub>17-skewing cocktail in the presence or absence of 1  $\mu$ M risankizumab, guselkumab, or tildrakizumab.<sup>31</sup> Accumulated cytokines were analyzed by multiplex assay at day 4 postdifferentiation. Treatment with control human IgG did not affect the release of T<sub>H</sub>17 cytokines (data not shown). Secretion of IL-17A, IL-17F and IL-22 into the supernatants was

greatly inhibited by risankizumab and guselkumab, while tildrakizumab showed only partial inhibition of IL-17 F and IL-22, and almost no inhibition of IL-17A secretion (Figure 4a). To gain a deeper understanding of the phenotypic changes that occur during this process, we performed standard flow cytometry and high-dimensional mass cytometry (CyToF) analysis on day 4 of the culture using a panel of antibodies as indicated (Supplemental Table S2). Consistent with the secreted cytokine levels in the supernatants, the frequencies of IL-17A<sup>+</sup> and IL-17 F<sup>+</sup> cells were significantly reduced by risankizumab and guselkumab, while tildrakizumab elevated the percentage of IL-17A<sup>+</sup> cells and only partially inhibited the differentiation of IL-17 F<sup>+</sup> T<sub>H</sub>17 cells (Figure 4b). It has been reported that the IL-23/T<sub>H</sub>17 axis plays a crucial role in regulating the immunopathogenesis of psoriasis, and IL-23R expression and signaling is a critical component of pathogenic T<sub>H</sub>17 cells.<sup>3,32,33</sup> We confirmed the surface expression of IL-23R in differentiated T<sub>H</sub>17 cells with an anti-IL-23R antibody (Supplemental Figure S8a). Risankizumab displayed a better inhibitory effect on the generation of IL-23R<sup>+</sup> T<sub>H</sub>17 cells than tildrakizumab, but similar or slightly better than guselkumab (Figure 4b).

To understand the effects of IL-23 signaling blockade on T<sub>H</sub>17 differentiation in more detail, a uniform manifold approximation and projection (UMAP) dimension reduction analysis was performed on day 0 (T<sub>H</sub>17 naive) and day 4 (T<sub>H</sub>17 control and risankizumab-, guselkumab- or tildrakizumab-treated) cells. PhenoGraph cell clustering revealed 28 populations within the T<sub>H</sub>17 cultures, and Wanderlust trajectory analysis indicated the likely path of differentiation of T<sub>H</sub>17 naive cells to T<sub>H</sub>17 cells *in vitro* (Figure 4c, Supplemental Figure S8b,c). Among the 28 clusters, distinct populations of terminally differentiated IL-17A<sup>-</sup>IL-17 F<sup>hi</sup> (cluster 26), IL-17A<sup>hi</sup>IL-17 F<sup>-</sup> (cluster 27) and IL-17A<sup>hi</sup>IL-17 F<sup>hi</sup> (cluster 28) cells were identified and were greatly reduced when cells were polarized in the presence of risankizumab or guselkumab (Figure 4c,d). In contrast, tildrakizumab had minimal impact on terminally differentiated T<sub>H</sub>17 cells by day 4 of culture, as its profile is nearly identical to the T<sub>H</sub>17 control UMAP plot (Figure 4d).

A heatmap of cluster frequencies provided an objective view of which treatments behaved most similarly with respect to the phenotypic distribution of cells in culture (Supplemental Figure S9a). Volcano plots showing differences in cluster frequencies as a ratio of the T<sub>H</sub>17 control were generated. In risankizumab- or guselkumab-treated cultures, cluster 26, 28

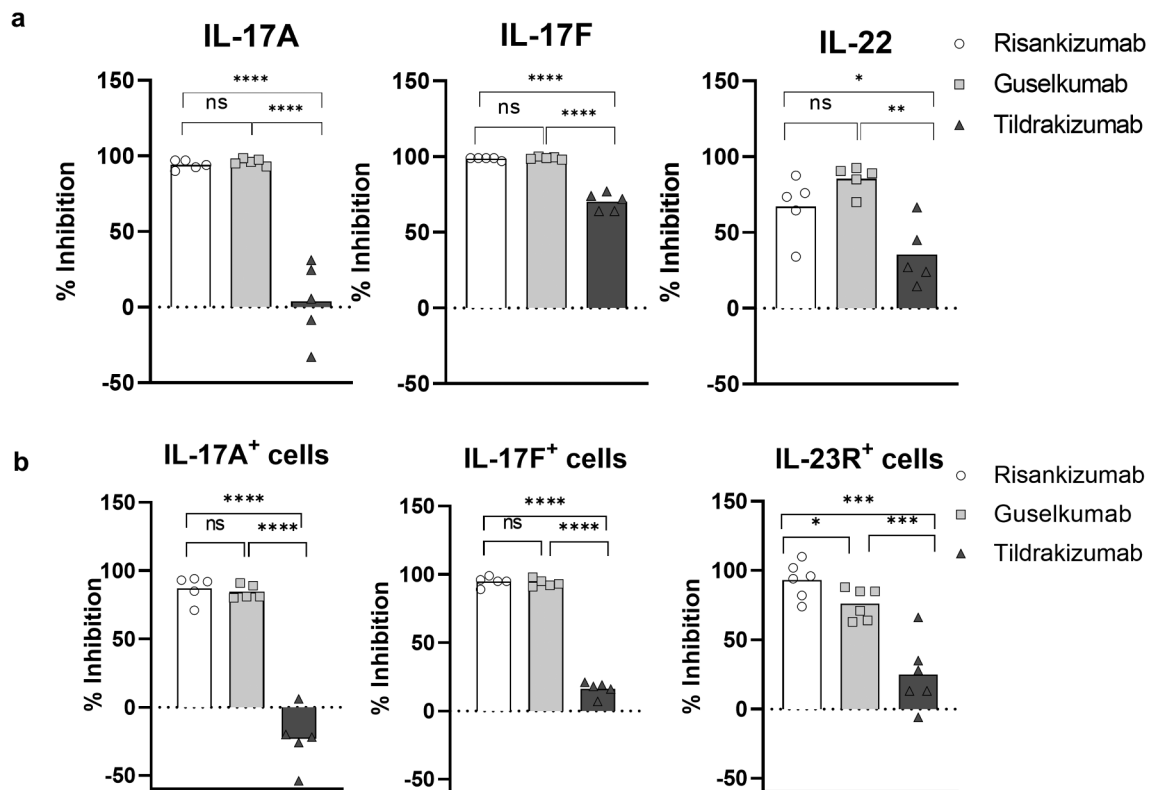


**Figure 4.** Treatment of naïve T cells in T<sub>H</sub>17 polarizing conditions with IL-23 antibodies results in loss of terminally differentiated IL-17<sup>+</sup> cells and accumulation of T<sub>H</sub>17 differentiation intermediates. (a) The inhibition of IL-17A, IL-17 F and IL-22 cytokine secretion by IL-23 antibodies at day 4 of T<sub>H</sub>17 polarization analyzed by multiplex. (b) The inhibition of IL-17A, IL-17 F, and IL-23 R expressing cells by IL-23 antibodies at day 4 of T<sub>H</sub>17 polarization analyzed by mass (IL-17A, IL-17 F; n = 5) or flow (IL-23 R; n = 6) cytometry. ns. not significant. \* p ≤ 0.05; \*\* p ≤ 0.01; \*\*\* p ≤ 0.005; \*\*\*\* p ≤ 0.001. (c) UMAP dimension reduction of all events from mass cytometry analysis of all day 4 treatment groups shows the landscape of populations arising during T<sub>H</sub>17 differentiation. PhenoGraph cell clustering identified 28 populations as shown in the legend. The Wanderlust algorithm was run using PhenoGraph population 2 as the seed population, and populations were then numbered according to the Wanderlust predicted order of differentiation. The red line indicates a likely path of differentiation. The terminally differentiated clusters expressing IL-17A (cluster 27), IL-17 F (cluster 26) or IL-17A and IL-17 F (cluster 28) are shown along with the expression of IL-17A and IL-17 F. (d) The UMAP plot of mass cytometry data from (c) is shown for individual treatment groups, which demonstrates the redistribution of populations as a result of treatment with IL-23 antibodies. Terminally differentiated IL-17<sup>hi</sup> clusters are highlighted with black rectangles. (e) Volcano plots show the fold change of PhenoGraph clusters following treatment with risankizumab compared to the T<sub>H</sub>17 control, guselkumab compared to the T<sub>H</sub>17 control, and risankizumab compared to guselkumab treatment. A false discovery rate (FDR) of 0.05 is shown with the dotted line to indicate the threshold for significant change. Populations that changed significantly are shown in green. n = 5 in c-e.

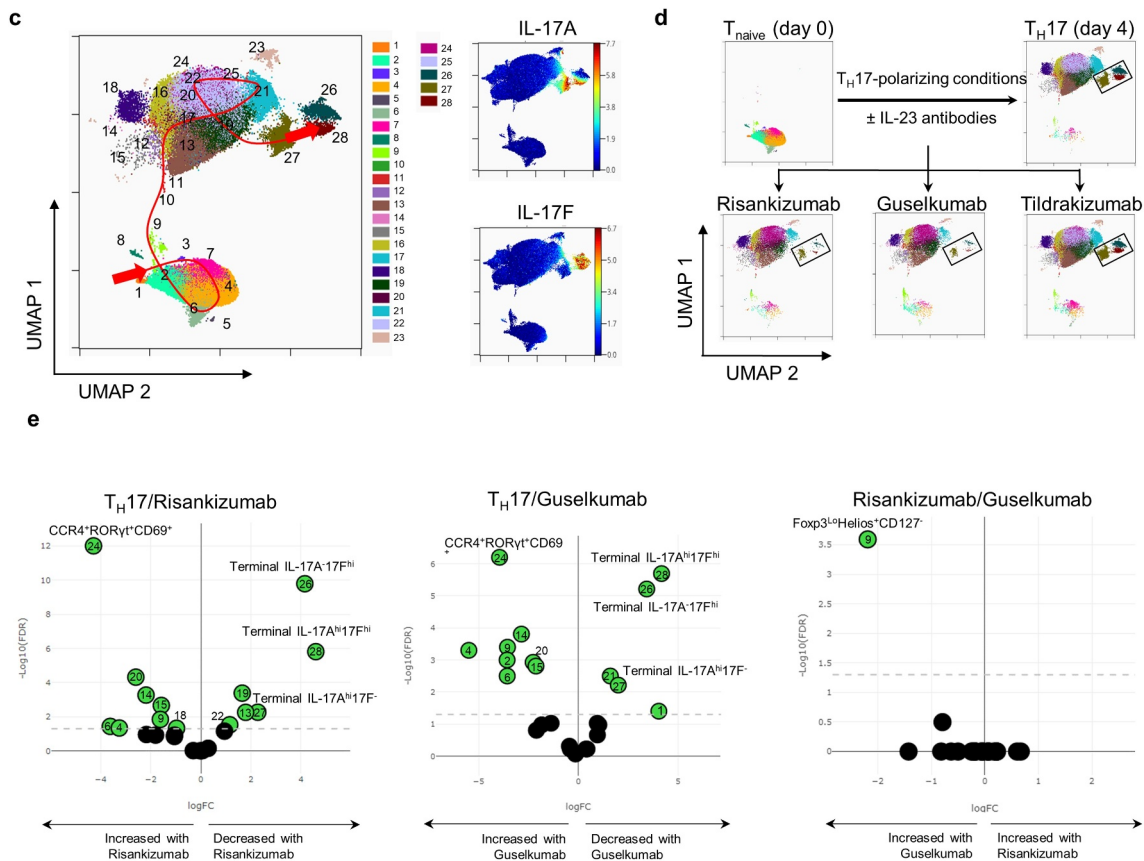


Figure 4. Continued.

and to a lesser extent cluster 27 were significantly decreased, while an intermediate  $CCR4^+ROR\gamma t^+CD69^+$   $T_H17$  population (cluster 24) had accumulated the most (Figure 4e). It is not known whether cluster 24 is a nonpathogenic  $T_H17$  subset or an intermediate population differentiating toward an IL-23-dependent pathogenic population. While treatment with risankizumab and guselkumab resulted in very similar phenotypic changes *in vitro*, one cluster was significantly different in frequency (Figure 4e). Cluster 9, an early differentiation intermediate with a Treg-like phenotype ( $Foxp3^{lo}Helios^+CD127^-$ ) accumulated more with guselkumab treatment than with risankizumab. In contrast to risankizumab and guselkumab, treatment with tildrakizumab only caused an increase in two very early differentiation intermediates,  $CCR6^-IL-23R^{lo}CD69^+$  (cluster 6) and  $CCR6^+IL-23R^-CD69^-$  (cluster 3) populations (Supplemental Figure S9b).

### **In vivo activity in IL-23-induced ear inflammation model**

We previously described a psoriasis-like skin inflammation model in C57BL/6 mice by daily intradermal injection of murine IL-23 into the ear.<sup>34,35</sup> This 5-d model demonstrates an IL-23-induced skin inflammation with increased ear thickness, leukocyte infiltration and elevated expression of IL-23/Th17 pathway genes, including IL-17A, IL-17 F, IL-22, S100A7a and  $\beta$ -defensin-4. The proinflammatory transcriptome of the model closely reflects the transcriptome of human psoriasis.<sup>34,36</sup> To investigate the effects of human IL-23 antibodies that do not cross-react with mouse IL-23,

a modification was made using intradermal injection of human IL-23 at 1  $\mu$ g/d for 4 d. The inflammation in response to human IL-23 injection was comparable to the murine IL-23-induced skin inflammation (Supplemental Figure S10).

To study the effects of risankizumab, guselkumab, tildrakizumab and ustekinumab on human IL-23-induced skin inflammation, dose response studies with the individual mAbs were conducted. Antibodies at doses of 0.01, 0.1, 1, 5 and 25 mg/kg were injected intraperitoneally (i.p.) 4 hours prior to the IL-23 ear injection on day 0 and day 2. Both risankizumab and guselkumab reduced IL-23-induced ear swelling in a dose-dependent manner (Figure 5a) at similar plasma concentrations (Table 4) and showed robust reduction in IL-23-induced proinflammatory and keratinocyte gene expression, including IL-17A, IL-22, S100A7a and  $\beta$ -defensin 4 (Figure 5b). At high plasma concentrations, in the range of 10–1000  $\mu$ g/mL, both risankizumab and guselkumab reduced IL-17A, IL-22, S100A7a and  $\beta$ -defensin 4 to a similar level (>70%). Surprisingly, risankizumab achieved a more pronounced reduction of the above gene expression than guselkumab at a lower plasma concentration of about 1  $\mu$ g/mL. In contrast to risankizumab and guselkumab, the impact of tildrakizumab and ustekinumab on IL-23 mediated skin inflammation was reduced. Tildrakizumab was ineffective in blocking both inflammation and gene expression changes, while ustekinumab generated a more modest response, marked by significant changes in ear thickness at only the highest dose

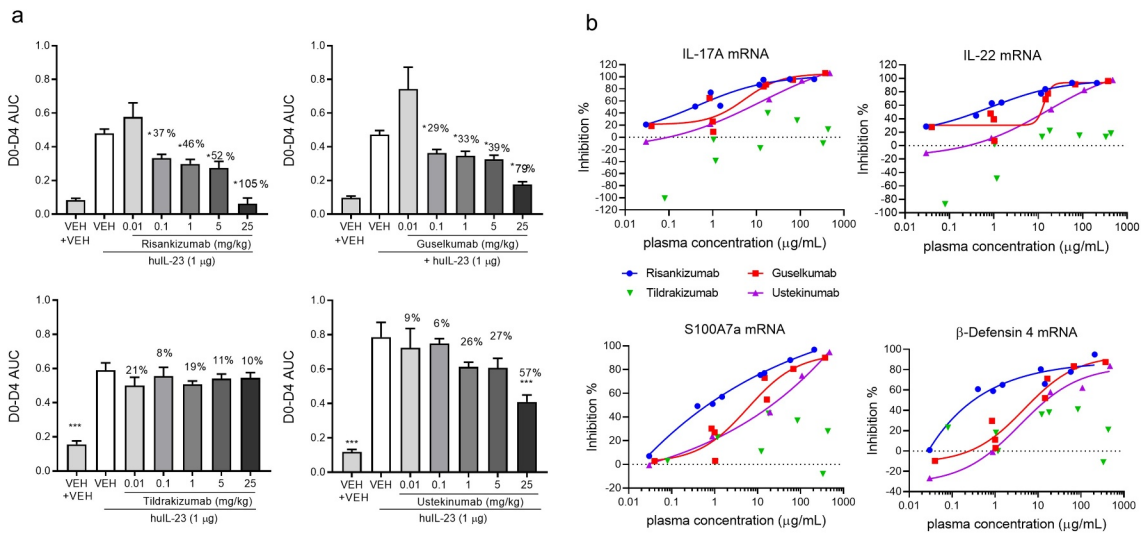


**Figure 5.** Risankizumab and guselkumab differentially inhibited IL-23 induced skin inflammation. (a) Ear swelling of vehicle- and IL-23-injected animals that were administered with either PBS (Veh+Veh) or various doses of antibodies are represented by day 0 to day 4 area under the curve ear thickness measurement (D0-D4 AUC). Data are shown as bar graph with mean + SEM. Values of mean percentages of inhibition (compared to the IL-23 injected alone animals) of the significantly reduced groups are also labeled on the graph. Data are pooled from two studies of four antibodies with total 11–12 animals in each dosing group. Significance was analyzed using one-way ANOVA with Tukey’s or Dunnett’s multiple comparison post hoc analysis. (b) The percentage inhibition of IL-17A, IL-22, S100A7a and  $\beta$ -Defensin 4 mRNA expression from (a) are plotted against the plasma concentrations of the antibody dosed groups in the IL-23 injected animals. Each point represents the mean values of the dosing group from pooled studies. Non-linear regression curve fittings of the four antibodies are also indicated on the plot using four parameter fit algorithm. (c) The percentage inhibitions of ear thickness AUC, and inhibition of IL-17A, IL-22, S100A7a and  $\beta$ -Defensin 4 mRNA expression from the head-to-head comparison studies between 0.1 mg/kg dosed risankizumab and guselkumab are plotted as bar graphs. Data are pooled from two studies with total 11–12 animals in each group and shown as mean + SEM. Significance was analyzed using two-way ANOVA with Sidak’s multiple comparison post hoc analysis. \*  $p \leq 0.05$ ; ns, no significance, i.e.,  $p > .05$ . (d) The percentage inhibition of IL-17A, IL-22, S100A7a and  $\beta$ -defensin 4 mRNA expression from individual animals of the head-to-head comparison studies that were dosed with antibodies at 0.1 and 1 mg/kg are plotted against the plasma concentrations of the antibodies of correlated animals. Data are pooled from two studies with 5–6 animals per group in each study.

**Table 4.** Antibody plasma concentrations ( $\mu\text{g/mL}$ ) in the IL-23 induced ear inflammation model.

Dose (mg/kg)	0.01	0.1	1	5	25
Risankizumab	$< 0.03^A$	$0.9 \pm 0.1$	$13 \pm 1.0$	$58 \pm 2.9$	$209 \pm 25$
Guselkumab	$0.04 \pm 0.003$	$1.0 \pm 0.05$	$16 \pm 0.7$	$68 \pm 4.4$	$374 \pm 9.1$

A. Exposure level of 0.01 mg/kg risankizumab was below the lowest level of detection limit at 0.03  $\mu\text{g/mL}$ . Data is presented as mean  $\pm$  SEM.

group. In addition, changes to gene expression were reduced in the ustekinumab-treated group, compared to risankizumab and guselkumab, at lower drug exposures.

In subsequent head-to-head studies, risankizumab and guselkumab were dosed at 0.1 and 1 mg/kg (achieving the targeted plasma concentrations of about 1  $\mu\text{g/mL}$  and 14  $\mu\text{g/mL}$ , respectively) to confirm and further investigate the differences between the observed efficacy at the lower plasma

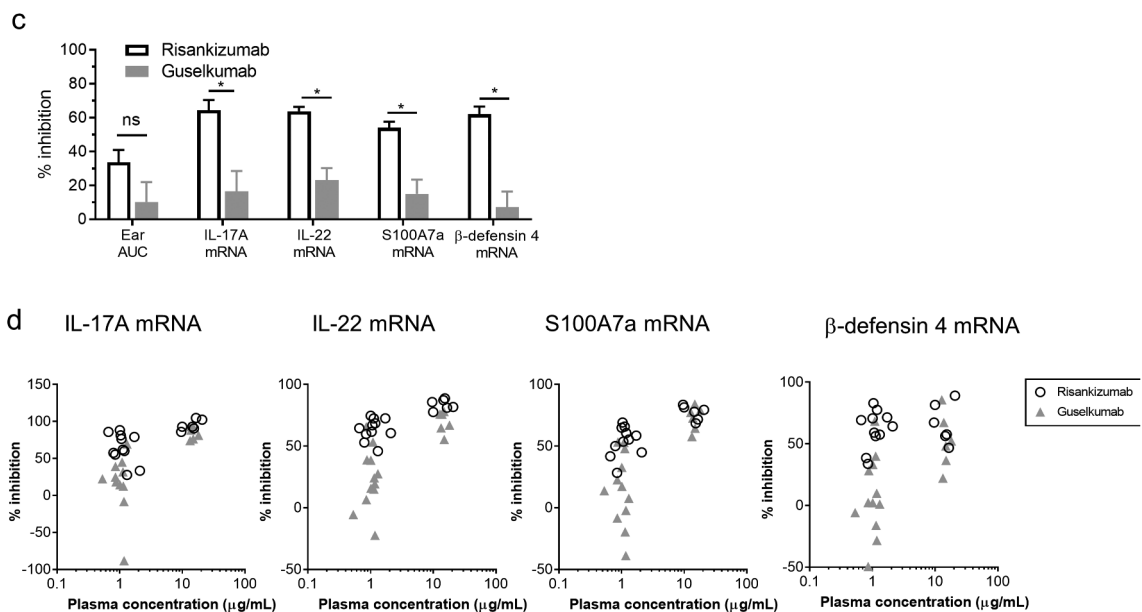


**Figure 5.** Continued.

exposure levels. At the 0.1 mg/kg dose, inhibition of IL-23-induced ear swelling trended higher (not significant) in risankizumab- (33%) than guselkumab- (10%) treated animals, while risankizumab reduced IL-17A, IL-22, S100A7a and  $\beta$ -defensin 4 gene expressions to a significantly greater extent than guselkumab (64%, 63%, 54% and 62% for risankizumab compared to 16%, 23%, 15% and 7% for guselkumab, respectively) (Figure 5c). Analysis of gene expression relative to antibody plasma concentrations revealed a more uniform inhibition of inflammatory gene expression with risankizumab at 1  $\mu$ g/ml compared to a greater range of inhibition in the guselkumab group. Meanwhile, the range of gene expression inhibition was more similar between risankizumab and guselkumab groups at the higher plasma concentration of about 14  $\mu$ g/mL (Figure 5d).

## Discussion

The antibodies that inhibit IL-23 through interaction with either the p19 or p40 subunit described in this study have all shown efficacy in patients with moderate or severe plaque psoriasis. Direct head-to-head clinical study between these antibodies has only been performed for risankizumab and ustekinumab, resulting in PASI 90 responses after 52 weeks of treatment of 81% for risankizumab vs 44% for ustekinumab.<sup>15</sup> It has been speculated that the lower response rate observed with ustekinumab may be due to the fact that ustekinumab, through its interaction with the p40 subunit, also inhibits IL-12. In contrast to IL-23, which stimulates IL-17 production by T lymphocytes, IL-12 has a regulatory role by specifically suppressing IL-17 secretion.<sup>37</sup> An alternate theory is that the difference in performance could be due to the lack of IL-39 inhibition. Any p40-specific antibody would not be able to inhibit this newly described cytokine comprising p19 (shared with IL-23) and EBI3 (shared with IL-27 and IL-35), which has been implicated in a mouse model of experimental lupus.<sup>38</sup> The existence of IL-39 in humans remains controversial, as some report that IL-39 has not been detected in humans and a recombinantly expressed version has no activity on human cells,<sup>39</sup> while others report upregulation and interaction of p19 and EBI3 in human keratinocytes stimulated with poly (I:C).<sup>40</sup> Whether human IL-39 exists and plays a role in the inflammatory disease process in psoriatic skin remains to be investigated.

The lower response rate observed with ustekinumab in psoriasis patients may also be partly due to suboptimal dose selection and its affinity for IL-23. Risankizumab has about 5-fold higher affinity than ustekinumab. Under equilibrium and nonsaturating dosing conditions, higher affinity antibodies bind more IL-23 until the affinity ceiling is reached.<sup>41</sup> Furthermore, the off-rate of the risankizumab/IL-23 complex is 10-fold slower than that of the ustekinumab/IL-23 complex, indicating that the risankizumab/IL-23 complex, once formed, is more stable.

The antibody affinities correlate with the *in vitro* bioactivities observed in STAT3 assays. For instance, in the whole blood STAT3 assay risankizumab and guselkumab had  $IC_{50}$ s of 6 pM and 10 pM, while tildrakizumab and ustekinumab had  $IC_{50}$ s of 39 pM and 40 pM. However, to achieve 80%

inhibition in the assay, the required concentrations were 12 pM for risankizumab, 20 pM for guselkumab, 195 pM for tildrakizumab and 246 pM for ustekinumab. These results show that risankizumab and guselkumab were able to reach their  $IC_{80}$  at concentrations that were only twice as high as their  $IC_{50}$ , whereas for tildrakizumab and ustekinumab the concentrations required to reach 80% inhibition were 5-fold higher than their  $IC_{50}$ , suggesting that to achieve full neutralization of IL-23 with a lower affinity antibody requires significantly higher antibody concentrations. Whether the requirement for significantly higher antibody concentration to achieve optimal IL-23 neutralization by ustekinumab and tildrakizumab translates to their performance in patients is not known and would require carefully controlled clinical studies. In this context, it is noteworthy that tildrakizumab's clinical efficacy at a 2-fold higher dose did not increase significantly (PASI 90 of 52–59% at 100 mg and 59% at 200 mg dose).<sup>13</sup>

Risankizumab and guselkumab inhibit the interaction of IL-23 with IL-23R $\alpha$  through competitive inhibition of IL-23, as neither shows simultaneous binding with IL-23R $\alpha$  to IL-23. In contrast, the tildrakizumab-bound IL-23 is still capable of binding to IL-23R $\alpha$ , albeit at a 200-fold weaker affinity. Indeed, tildrakizumab's epitope on IL-23 does not have any overlapping residues with the IL-23R $\alpha$  interaction site. These data suggest that tildrakizumab may be an allosteric inhibitor of IL-23. In the HEK293 cell-binding study, the tildrakizumab/IL-23 complex did not show binding to the cells expressing IL-23R $\alpha$ . Given the weak affinity between the tildrakizumab/IL-23 complex and IL-23R $\alpha$  ( $K_D$  = 190 nM), little binding on HEK293 cells is expected at the cytokine concentrations tested (<20 nM). It is not clear whether tildrakizumab's inhibition of IL-23 signaling is negatively affected by its epitope on IL-23.

Bloch et al. reported that the assembly of the IL-23 ternary complex follows a typical two-step heterodimeric receptor activation mechanism in that IL-23 binds to IL-23R $\alpha$  first followed by the recruitment of IL-12R $\beta$ 1.<sup>29</sup> The binding affinities as measured using isothermal titration calorimetry (ITC) were  $K_D$  ITC = 44 nM for the interaction of IL-23 with IL-23R $\alpha$  and  $K_D$  ITC = 25 nM for the subsequent recruitment of IL-12R $\beta$ 1, while the interaction of IL-23 through its p40 subunit with IL-12R $\beta$ 1 was very low affinity with  $K_D$  ITC = 2  $\mu$ M.<sup>29</sup> In our study, we determined the binding affinities of IL-23 with individual receptor subunits using SPR to be 0.8 nM for IL-23/IL-23R $\alpha$  and 19 nM for IL-23/IL-12R $\beta$ 1. The difference in affinities from the two studies may be due to the use of different recombinant protein material and methods applied. Others have reported the affinity of the interaction between IL-12 through its p40 subunit and IL-12R $\beta$ 1 to be in the low nanomolar range.<sup>42</sup>

Using HEK293 cells expressing the individual receptor subunits, we investigated whether antibody/IL-23 complexes (comprised of 10 nM antibody and 5–20 nM IL-23) were able to bind to the individual receptor subunits. Ustekinumab/IL-23 showed strong binding to IL-23R $\alpha$  expressing cells, while guselkumab/IL-23 and tildrakizumab/IL-23, respectively, showed strong and moderate binding to the IL-12R $\beta$ 1-expressing cells. In contrast, risankizumab/IL-23 showed a very low binding to IL-12R $\beta$ 1 and no binding to IL-23R $\alpha$ -expressing cells, suggesting that risankizumab/IL-23

complexes do not interact with IL-23 receptor-expressing cells. In addition, risankizumab has reduced binding to the high-affinity FcγRs and undetectable binding to the low-affinity FcγRs due to the L234A, L235A mutations in the hinge. Nevertheless, it is not clear whether the almost complete lack of cell surface receptor interaction by risankizumab has any impact on its effectiveness, mechanism of action or tissue distribution.

In the *in vivo* studies using an IL-23-mediated psoriasis-like skin model in mice, we demonstrated differential outcomes with respect to the efficacy driven by risankizumab, guselkumab, tildrakizumab and ustekinumab. Compared to tildrakizumab and ustekinumab, both risankizumab and guselkumab were able to robustly inhibit IL-23-induced ear swelling and pathway gene expression of IL-17A, IL-22, S100A7a and β-defensin 4. Surprisingly, while both risankizumab and guselkumab achieved comparable systemic exposure levels at any given dose, at the lower dose of 0.1 mg/kg, where plasma concentrations were about 1 μg/mL, risankizumab showed significantly greater inhibition of IL-23 pathway gene expression than guselkumab. This is of particular interest, as in the clinical setting the human trough plasma concentrations of risankizumab and guselkumab are about 1–2 μg/mL as indicated in the approved labels. Further investigation revealed that the higher extent of inhibition by risankizumab compared to guselkumab was not due to the L234A, L235A mutations in the risankizumab hinge region, as a non-mutated IgG1 form of risankizumab also showed similar inhibition at a dose of 0.1 mg/kg (data not shown).

One potential explanation for the differential gene expression effect of risankizumab over guselkumab, at 0.1 mg/kg, is the tissue distribution of these antibodies. In an exploratory study, we observed greater accumulation of risankizumab than guselkumab in the diseased ear tissue at 48 hours post-dosing (Supplemental Figure S11a,b). The increased accumulation of risankizumab was dependent on IL-23-induced inflammation, as risankizumab did not accumulate in the non-inflamed contralateral ear of the same animal. While the accumulation of antibodies in the ear could only be measured in animals dosed at 1 mg/kg due to the limitation of the detection method, it is tempting to speculate that at 0.1 mg/kg dose there is a connection between the extent of skin tissue distribution of risankizumab and its impact on reducing IL-23 pathway gene expression.

Our *in vitro* T<sub>H</sub>17 differentiation assay provided a unique insight into the effect of IL-23 neutralization on the development of different cell populations along the differentiation path from naïve T cells to T<sub>H</sub>17 cells. Risankizumab and guselkumab had very similar effects on the inhibition of T<sub>H</sub>17 cell differentiation, showing significantly decreased IL-17A, IL-17 F, and IL-22 secretion and inhibition of the terminal T<sub>H</sub>17 subset formation, while tildrakizumab had very little effect on T<sub>H</sub>17 cell differentiation and only partially accumulated very early T<sub>H</sub>17 intermediates with low IL-23R expression. Using CyTOF analysis, it appeared that risankizumab and guselkumab had a greater effect on IL-17 F<sup>+</sup> than IL-17A<sup>+</sup> cells, suggesting that the IL-17 F<sup>hi</sup> subsets (IL-17A<sup>+</sup>F<sup>hi</sup> and IL-17A<sup>+</sup>F<sup>hi</sup>) could be the initial T<sub>H</sub>17 populations affected by IL-23 neutralization. *In vitro* IL-23 neutralization also caused

a shift toward the adoption of alternate T helper pathways. For instance, we observed an increase in Foxp3 and Gata3 expression in cultures treated with either risankizumab or guselkumab (data not shown), while Cluster 9, an early differentiation intermediate with a Treg-like phenotype (Foxp3<sup>lo</sup>Helios<sup>+</sup>CD127<sup>-</sup>) accumulated more with guselkumab treatment than with risankizumab treatment. This suggests that cells may be re-routed toward a Treg-like lineage upon IL-23 neutralization.

Tildrakizumab's poor inhibition in the 4-d T<sub>H</sub>17 differentiation assay and the 4-d *in vivo* mouse ear swelling model was surprising in light of its sub-nanomolar binding affinity to IL-23 and bioactivity in whole blood. Tildrakizumab inhibits human IL-23 activation of mouse splenocytes *in vitro* as described in patent US8293883B2, and we confirmed that active tildrakizumab was present in the mouse sera at the end of the study, suggesting that in these studies of longer duration tildrakizumab is not able to effectively inhibit IL-23 signaling, potentially due to its epitope and unusual mechanism of inhibition.

Overall, our study results indicate that the four clinically approved antibodies ustekinumab, guselkumab, tildrakizumab, and risankizumab differ in affinity for IL-23 and binding epitopes. These key attributes contribute to differences in *in vitro* potency affecting STAT3 signaling and T<sub>H</sub>17 cell differentiation, receptor interaction inhibition mode and *in vivo* efficacy in the mouse ear inflammation model. Carefully planned clinical studies are required to further investigate the impact of observed pre-clinical differences on these drugs' clinical performance.

## Materials and methods

### Proteins, cell lines and human specimen materials

Human single-chain (sc) IL-23 (IL-12p40<sub>(23-328)</sub>-(GGGGS)×4-IL-23p19<sub>(21-189)</sub>-TEV-FLAG-8His based on UniProt (P29460, Q9NPF7)) was expressed in HEK293 cells and purified using HisTrap FF (GE) and Superdex 200. Heterodimeric human IL-23 was purchased from ThermoFisher (cat. No. 14-8239-63). Human IL-23Ra protein was purchased from LSBio (LS-G40259-50). Human IL-12Rβ1-Fc was purchased from R&D system (ays0619011). The anti-IL-23R antibodies 20E5 and 3C11 were expressed in HEK293 cells.<sup>43</sup> Clinical-grade ustekinumab, guselkumab and tildrakizumab were purchased from Clinigen Inc. Risankizumab was produced as a clinical drug substance at Boehringer Ingelheim. An in-house produced version of ustekinumab, with equal potency compared to clinical-grade ustekinumab, was used in the mouse ear-swelling model. Control human IgG1 (anti-tetanus toxoid and anti-CMV) was expressed in HEK293 cells.

Stable HEK293 cell lines expressing human IL-23Ra (NP\_653302) with an N-terminal HA tag and/or human IL-12Rβ1 (NP\_005526.1) were generated using standard procedures.<sup>44</sup> The expression levels of IL-23Ra and IL-12Rβ1 were measured by FACS using anti-HA-PE and anti-CD212-APC antibodies (Miltenyi Biotec), respectively.

### Thermostability assays and forced degradation studies of deamidation prone sequences

DSC and nanoDSF measurements were performed as previously described.<sup>45</sup> Briefly, antibody samples were prepared at a concentration of 1 mg/mL in 4.4 mM Succinate, 225 mM Sorbitol, 0.02% Polysorbate 20, pH 6.0 (risankizumab) or 3.87 mM L-histidine, 7.15 mM L-histidine monohydrochloride monohydrate, 7.9% w/v sucrose, 0.05% w/v polysorbate 80, pH 5.8 (ustekinumab, guselkumab, and tildrakizumab). The thermal ramps were performed from 20°C to 95°C with a scan rate of 1°C/min. DSC thermograms were normalized by concentration and fitted to three peaks using a non-two-state unfolding model. Unfolding transition points

( $T_{\text{onset-DSC}}$  and  $T_m$ ) were determined using MicroCal PEAQ-DSC software.  $T_{\text{Agg}}$  was obtained by monitoring the back-reflection of near ultraviolet (UV) light using back reflection optics in Prometheus NT.48 with Prometheus PR. Control software (NanoTemper Technologies).

Guselkumab was incubated at 5 mg/mL in 0.1 M Tris buffer pH 8.0 for up to 10 d. The samples were digested and peptides were analyzed by LC-MS to assess deamidation.

### Affinity and kinetics measurement by SPR

Binding kinetics of IL-23 antibodies for recombinant human sc or heterodimeric IL-23 were determined by SPR at 37°C using an anti-Fc capture assay approach as described.<sup>45</sup> Briefly, IL-23 antibodies were captured on an anti-human Fc chip. IL-23, ranging in concentration from 36 nM to 0.15 nM in a randomized 3-fold dilution series, was injected over both reference and test surface for 5 minutes at 50  $\mu\text{L}/\text{minute}$ . The dissociation was monitored for 1 hour at 50  $\mu\text{L}/\text{minute}$ . Data were double referenced and fitted globally to a 1:1 binding model using Biacore T200 Evaluation software to determine the binding kinetic rate constants  $k_a$  ( $\text{M}^{-1}\text{s}^{-1}$ ) and  $k_d$  ( $\text{s}^{-1}$ ) and the equilibrium dissociation constant  $K_D$  (M). Mean and standard deviations from 5 (scIL-23) or 3 (heterodimeric IL-23) independent experiments are reported.

### FcRn affinity chromatography

FcRn column chromatography was performed essentially as described.<sup>46</sup> Briefly, FcRn/ $\beta 2$  microglobulin was expressed, purified, biotinylated and coupled to streptavidin sepharose. The resin was packed into a Tricorn 5/50 column (GE Healthcare) and equilibrated with 20 mM MES buffer, 150 mM NaCl, pH 5.5. Antibody samples (100–250  $\mu\text{g}$ ) were adjusted to pH 5.5 by dilution with equilibration buffer and applied to the FcRn column using the AKTA Pure system at a flow rate of 0.25 mL/min. The column was washed with 10 mL equilibration buffer. Antibodies were eluted with a linear pH gradient to 20 mM Tris, 150 mM NaCl, pH 8.8, within 120 mins.

### In vitro bioassay with IL-23-induced human whole blood

Whole blood from three healthy human donors was obtained through Sanguine Biosciences in K3EDTA Vacuette® tubes (Greiner, 455036). Donors were selected based on whole-blood response to scIL-23 stimulation to ensure at least 5-fold

increase of pSTAT3 expression compared to unstimulated samples. Test antibodies were serially diluted and preincubated with 10 ng/mL IL-23 in phosphate-buffered saline (PBS) supplemented with 1% bovine serum albumin (BSA) at 37°C for 1 hour. The antibody/IL-23 complex was diluted 10-fold with 200  $\mu\text{L}$  human whole blood such that the final concentration of IL-23 was 1 ng/mL, and the antibody concentrations ranged from 20 nM to 0.076 pM. Anti-CD161-Alexa Fluor 647 (BioLegend, 339910) was added to the reaction and incubated for 20 minutes at 37°C. Reaction was stopped by adding Phosflow lyse/fix buffer (BD Biosciences, 558049). Cells were permeabilized using 90% methanol/10% water (Honeywell) and washed with PBS supplemented with 1% BSA. Cells were stained with anti-CD45 PerCp/Cy5.5 (BioLegend, 304028) and anti-pSTAT3 PE (pY705) (BD Biosciences, 562072). Samples were acquired on a FACSCanto II using DIVA software (BD Biosciences). pSTAT3 fluorescence intensity in CD45<sup>+</sup>CD161<sup>hi</sup> cells was analyzed using FlowJo software (BD Biosciences). The data were expressed as percentage control response where unstimulated samples were defined as 0% and IL-23 stimulated samples without added antibodies were defined as 100%. IC<sub>50</sub> and IC<sub>80</sub> values were calculated using a four-parameter equation by Prism 8 software (GraphPad Software).

### In vitro bioassay with IL-23 receptor expressing cell line

A cell-based reporter gene assay (RGA) was developed by transiently overexpressing the two subunits of the IL-23 receptor (IL-12R $\beta 1$  and IL-23R $\alpha$ ) in a commercially available HeLa (human epithelial) cell line stably expressing a STAT3-linked firefly luciferase response element (Signosis Inc). IL-23R HeLa STAT3 luciferase cells were thawed and maintained in growth media (DMEM media supplemented with D-glucose 4.5 g/L, L-glutamine 2 mM, sodium pyruvate 1 mM, 10% fetal bovine serum (FBS)) at 37°C in a 5% CO<sub>2</sub> incubator. A 3-fold serial dilution of IL-23 mAbs in growth media was pre-incubated with an equal volume of 4 ng/mL human scIL-23 for 1 hour in a dilution plate (Costar). Fifty microliters of the mAbs/IL-23 complexes were added in triplicate to wells of a 96-well white assay plate (Nunc) and IL-23R HeLa STAT3 luciferase cells (25,000 cells in 50  $\mu\text{L}$ ) were added to each well. The final concentration of IL-23 was 1 ng/mL (17.4 pM) alone or with a titration curve of antibodies ranging from 3 nM to 0.15 pM (risankizumab, guselkumab, control human IgG) or from 27 nM to 1.4 pM (tildrakizumab and ustekinumab). Assay plates were incubated for 5 hours at 37°C, 5% CO<sub>2</sub>, transferred to room temperature and 100  $\mu\text{L}/\text{well}$  of One Glo Luminescence substrate (Promega) was added. The plates were covered with foil to block the light and sealed with a plate sealer. Plates were shaken for at least 2 minutes on a plate shaker to mix and lyse the cells before the readout on a Microbeta2 luminometer (Perkin Elmer). IC<sub>50</sub> and IC<sub>80</sub> values were calculated as indicated in the whole blood assay.

### Epitope mapping by HDX-MS

All HDX-MS experiments were performed using a nanoACQUITY UPLC system with HDX technology (Waters Corporation). Forty micromolar of scIL-23 was

incubated with or without 40  $\mu\text{M}$  of guselkumab in equilibration buffer (10 mM potassium phosphate, pH 7.2). 6  $\mu\text{L}$  of the samples were diluted with 54  $\mu\text{L}$  equilibration buffer or deuterated labeling buffer (10 mM potassium phosphate buffer, pH 7.2) in triplicates at 20°C for different periods of time: 0 second, 10 seconds, 1 minute, 10 minutes, 1 hour and 10 hours. The sample was quenched with 50  $\mu\text{L}$  of quench buffer (100 mM potassium phosphate, 4 M guanidine hydrochloride and 500 mM TCEP, pH 2.4) and incubated for 10 minutes at 1°C. A total of 100  $\mu\text{L}$  quenched sample was injected into UPLC equipped with an Enzymate™ BEH pepsin column (2.1 mm  $\times$  30 mm, Waters Corporation) for online digestion at 15°C. The desalting and separation were carried out at 0.2°C using a BEH C18 VanGaurd™ pre-column (2.1 mm  $\times$  5 mm, 1.7  $\mu\text{m}$ , Waters Corporation) and an ACQUITY BEH C18 analytical column (1.0 mm  $\times$  100 mm, 1.7  $\mu\text{m}$ , Waters Corporation). Peptides were separated using a 12-minute linear acetonitrile gradient (5–40%) containing 0.1% formic acid at 40  $\mu\text{L}/\text{minute}$ . The eluent was directly sprayed into a Synapt G2 mass spectrometer (Waters Corporation) with electrospray ionization and lock-mass correction using Leu-Enkephalin solution. Mass spectra were acquired in MSE mode with ion mobility over an  $m/z$  range of 50 to 2000. Blanks of 0.1% formic acid in water were injected in between each LC-MS run using the same analytical gradient to minimize the carry-over. All peptides were identified from non-deuteration controls using ProteinLynx Global Server 3.0.2 software (Waters Corporation). Deuterium uptake for each peptide was determined based on the difference between the centroid of the isotopic distribution of undeuterated and deuterated samples using DynamX 3.0 software (Waters Corporation). Potential epitope is determined if the deuterium uptake difference exceeds 0.5 Da for a single time point and 1.1 Da for the sum of deuterium uptake differences of 5 HDX time points. All spectra and data processing were manually confirmed and validated for epitope identification.

### **Binding mode characterization of IL-23 antibodies**

To investigate whether antibody-bound IL-23 still binds IL-23Ra, the SPR assay format was set up with the following four steps. First, the anti-IL-23R antibody 20E5, which is noncompetitive with IL-23 binding to IL-23Ra, was covalently immobilized on the CM5 biosensor chip via amino groups. IL-23 R antibody 20E5 (25  $\mu\text{g}/\text{mL}$ ), diluted in 10 mM sodium acetate, pH 4.5, was injected for 420 s across the activated surface. Approximately 10,000 RU of IL-23 Ra antibody 20E5 was immobilized on the chip surface on flow cells 2, 3, and 4. A modified CM surface with similarly conjugated control human IgG antibody in flow cell 1 was used as a reference surface. Second, human IL-23 Ra protein at 100 nM in HBS-EP+ was injected for 60 s over the IL-23 Ra antibody coated surface. Third, human IL-23 at 30 nM and test antibodies at 300 nM (saturating concentration) were equilibrated in HBS-EP+ at 25 °C for 5 hours and were injected for 120 s, followed by 60 s dissociation in HBS-EP+ at a flow rate of 50  $\mu\text{L}/\text{minute}$ . Fourth, the surface was regenerated by injection of 10 mM glycine-HCl pH1.5 over the test and reference flow cells.

The binding kinetics of IL-23 and IL-23 Ra was assessed in the presence of tildrakizumab. The assay format was according to the following four steps: 1) capture of tildrakizumab onto a testing flow cell of an anti-human Fc chip and reach a density of about 1500 RU; 2) load scIL-23 or heterodimeric IL-23 to test flow cell to a density of around 150 RU; 3) analyte injection (IL-23 Ra or buffer) over both reference and test surface, 150  $\mu\text{L}$  at 50  $\mu\text{L}/\text{minute}$ , after which the dissociation was monitored for 10 minutes at 50  $\mu\text{L}/\text{minute}$ ; 4) regeneration of capture surface by 10 mM glycine-HCl, pH 1.5 injections over both reference and test surface. IL-23 Ra injections ranged in concentration from 100 nM to 1 nM in a randomized 3-fold dilution series. The binding kinetics of IL-23 and IL-23 Ra without tildrakizumab was measured by capturing IL-23 Ra onto a chip with the anti-IL-23 R antibody 20E5 to a ligand density of 100 RU. Analyte (IL-23 or buffer) was injected from 300 nM to 4 nM in a 3-fold dilution series. All other parameters were the same as described above.

To investigate whether antibody-bound IL-23 binds to IL-12R $\beta$ 1, 300 nM of IL-23 and 900 nM of antibodies were equilibrated in HBS-EP+ at 25°C for 5 hours. The complex was then injected onto a chip surface where IL-12R $\beta$ 1-Fc was covalently linked through amine chemistry on flow cell 2. Biacore 8 K was used for data collection. The active flow cell 2 signal was referenced against flow cell 1 without IL-12R $\beta$ 1-Fc.

IL-23/antibody complex binding to IL-23 receptor was also evaluated on HEK293 cells. IL-23 antibodies and control human IgG1 antibody were labeled with Zenon antibody labeling technology (Thermo Fisher Scientific) according to the manufacturer's instructions. IL-23/antibody complexes were prepared by mixing 10 nM labeled antibody with human IL-23 at concentrations of 0, 1.25, 2.5, 5, 10, and 20 nM in MACS cell separation buffer (Miltenyi Biotec), resulting in antibody-binding site/IL-23 molar ratios of 1:0, 16:1, 8:1, 4:1, 2:1, and 1:1, respectively. IL-23/antibody mixtures were pre-incubated on ice for 1 hour. The cells were plated in 96-well round-bottom plates (Corning) at 200,000 cells per well and washed once with MACS cell separation buffer. IL-23/antibody complex (100  $\mu\text{L}/\text{well}$ ) were added and incubated for 1 hour on ice. Cells were washed twice with 200  $\mu\text{L}$  MACS cell separation buffer, and IL-23/antibody binding was assessed by FACS (BD Accuri C6) and analyzed by FlowJo V10.

### **T<sub>H</sub>17 differentiation assay**

Mononuclear cells were prepared from human cord blood (LifeSouth Community Blood Centers) on Ficoll-Paque gradients, and naïve CD4<sup>+</sup> T cells were isolated using an EasySep Human Naïve CD4<sup>+</sup> T cell isolation kit (StemCell). To generate T<sub>H</sub>17 cells, naïve CD4<sup>+</sup> T cells were activated with anti-CD3/CD28-coated beads (Gibco) in X-VIVO 20 serum-free hematopoietic cell media (Lonza) and cultured for 4 d in the presence of a T<sub>H</sub>17-skewing cocktail containing 10 ng/mL hTGF- $\beta$ , 10 ng/mL hIL-1 $\beta$ , 10 ng/mL hIL-2, 1  $\mu\text{g}/\text{mL}$  anti-hIL-4, 1  $\mu\text{g}/\text{mL}$  anti-hIFN- $\gamma$  (R&D Systems) and 10 ng/mL human scIL-23. To assess the effect of anti-IL-23 antibodies on T<sub>H</sub>17 cell differentiation, risankizumab, guselkumab, tildrakizumab, or control human IgG (1  $\mu\text{M}$ ) was added into the culture on day 0.

Harvested supernatants secreted from cells at indicated time-points were subjected to cytokine quantification with the Multiplex Assay Kit (EMD Millipore). Cells were stained with LIVE/DEAD Fixable Blue (Thermo Fisher Scientific), followed by Human TruStain FcX Fc Receptor Blocking Solution (BioLegend). Surface staining was performed by incubation with PE/Cyanine7 anti-human CD196 (CCR6) antibody (BioLegend) and biotinylated anti-IL23R antibody (3C11) on ice for 1 hour, followed by Alexa Fluor 647 Streptavidin (BioLegend) for an additional 30 minutes on ice. Flow cytometric measures were performed on LSRFortessa (BD Biosciences) and analyzed using FlowJo software (BD Biosciences). Percent (%) inhibition of the secreted cytokines is calculated in the comparison of cytokine from the T<sub>H</sub>17-only group with those from anti-IL23 antibodies-treated groups after subtraction of day 0 level. Similarly, percentage inhibition of the frequency of IL-23 R<sup>+</sup> cells is calculated based on differences between with and without anti-IL23 antibodies-treated groups after the subtraction of the frequency of different subsets from day 0 samples.

### CyTOF assays

Metal-conjugated antibodies were purchased from Fluidigm or conjugated using the MaxPar X8 antibody-labeling kit (Fluidigm) according to manufacturer instructions.

Thirty minutes prior to harvesting cell cultures, 5-Iodo-2'-deoxyuridine (IdU) (Fluidigm) was added to cell cultures to identify cells in S-phase. Dead cell staining was done by resuspending samples in 1 mL of Fluidigm cell staining buffer (CSB) along with 1  $\mu$ L of Cell-ID Cisplatin (Fluidigm), incubating for 30 seconds followed by 2 washes with 2 mL of CSB. For intracellular staining, the eBioscience Foxp3 staining set (Thermo Fisher) was used according to their protocol, except a 20-minute incubation with Fixation/Permeabilization reagent was used instead of the recommended 30 minutes to minimize impact on sensitive cell surface epitopes. Both surface and intracellular staining were carried out at room temperature for 30 minutes, followed by 2 washes with 2 mL of CSB. Following intracellular staining samples were fixed with 1 mL of 4% paraformaldehyde for 15 minutes. Cell intercalation with natural abundance iridium was done according to the Fluidigm protocol and incubated overnight. To bank cells at  $-80^{\circ}\text{C}$  so that cells could be acquired in batches, intercalated cells were washed twice with 2 mL CSB and then resuspended in 0.5 mL of cell freezing solution (FBS with 10% DMSO) and stored at  $-80^{\circ}\text{C}$  until acquisition.

The frozen samples were thawed quickly in 2 mL of CSB and centrifuged at  $600 \times g$ . Samples were then washed and centrifuged two more times in Cell Acquisition Solution (Fluidigm) and left pelleted until acquisition. Prior to sample acquisition, the Helios mass cytometer was tuned using Tuning Solution (Fluidigm) and the tuning protocol in version 6.7.1014 of the CyTOF-installed software. Immediately prior to acquisition, samples were resuspended in 1 mL of Cell Acquisition Solution containing EQ Four Element Calibration Beads (Fluidigm). As many events as possible were collected for each sample, up to a limit of  $10^5$  cells/sample. Following acquisition, samples were normalized to the EQ Four Element Calibration Beads using the CyTOF-installed software.

After gating on viable singlet cells in Cytobank, all subsequent analysis was done in OMIQ. The percentage inhibitions of the frequency of IL-17A<sup>+</sup> and IL-17 F<sup>+</sup> cells were calculated using the same formula used for IL-23 R<sup>+</sup> cells. The dimension reduction algorithm UMAP was run on all files using markers indicated in the antibody panel (Supplemental Table S2). The default OMIQ settings were used for all algorithmic analysis. PhenoGraph cell clustering was then performed on all files using the same markers as used for the dimension reduction. Following cell clustering, the trajectory inference algorithm Wanderlust was run on just day 0 and T<sub>H</sub>17 control files. The same markers used for the dimension reduction were used for trajectory inference. PhenoGraph cluster 2 was used as a starting point because it was the most abundant cluster represented in the day 0 sorted naïve CD4<sup>+</sup> T cells. The EdgeR tool in OMIQ was used to create volcano plots to identify significantly different cluster frequencies between two groups.

### Animal models

Wild-type female C57BL/6 mice, 8–12 weeks of age (18–22 g) were purchased from Charles River Labs. Animals were housed in a pathogen-free environment of an American Association for Accreditation of Laboratory Animal Care-approved facility, five per cage on aspen chip bedding (Sanichip) with individual ventilation and were kept in a room with an average temperature of 72°F on a 12-hour light-dark cycle. The mice had free access to diet (2014 Teklad global 14% protein rodent diets from Envigo), and water. The animals were acclimated to laboratory conditions for at least 1 week before the testing. All studies were conducted in a blinded manner.

IL-23-induced skin inflammation model was similar to previously described with slight modification.<sup>35</sup> In brief, 1  $\mu$ g human recombinant IL-23 (AbbVie) solution or sterile PBS + 0.1% BSA (vehicle) was intradermally injected into the dorsal side of a single ear in an isoflurane-anesthetized mouse with a 32-gauge needle, once a day for four consecutive days starting on day 0. Ear thickness was measured daily and mice were then humanely euthanized on day 4 for tissue harvesting. To assess the effect of antibodies, i.p. injections of various doses of IL-23 antibodies and control human IgG1 (human anti-CMV) were performed on day 0 and day 2, 4 hours prior to the IL-23 ear injection.

### Measurement of gene expression

Animal whole ears were homogenized, and the expression of various genes was determined using QuantiGene multiplex kit (ThermoFisher Scientific). All procedures followed manufacturer's instructions. Data were acquired using FlexMAP 3D cytometer (Luminex). All data were normalized by GeoMean to two housekeeping genes, Hprt and Gapdh. Normalized data were then compared to the control group (i.e., vehicle-treated Sham animals) and fold changes were calculated. The fold changes were then used to calculate the percentage of inhibition for the genes of interest.

Probe sets used in the Quantigene multiplex analysis were designed by the vendor. Detailed information about the genes that were measured is listed in Supplemental Table S3.

### Histology and immunohistochemistry

Collected ears were fixed in 4% paraformaldehyde for 20 hours at room temperature, transferred to 30% sucrose at 4°C for at least 24 hours and embedded in Tissue-Tek OCT Compound. Tissue blocks were stored at -80°C. Immunohistochemistry (IHC) was performed on fixed frozen 5 µm sections using a Leica Bond RX Fully Automated Research Stainer (Leica Biosystems) at ambient temperatures. Following a series of washes and pretreatments with dual endogenous block (Dako), 70% methanol in 3% hydrogen peroxide (freshly made), Protease I (Ventana) and Protein Blocks (Dako), tissue sections were incubated with 0.5 µg/ml purified rabbit anti-human or the negative isotype control rabbit anti-hamster IgG (H + L) mouse adsorbed antibody (Southern Biotech). Antibody binding was detected with Bond Polymer Refine Red detection using alkaline phosphatase-linked compact polymer and visualized with Leica red (Leica Biosystems). Slides were then counterstained with hematoxylin.

### IHC image acquisition and quantification

Slides were imaged using the Panoramic 250 whole slide scanner at 20× magnification (3D Histech). Image analysis (IA) was performed on the digitized images to quantitate the extent of dosed antibody in the ear tissue. The IA involved a three-step algorithm approach using Visiopharm software (VisioPharm). The first algorithm isolated the tissue from the background and delineated the tissue as a ROI (Region of Interest) around the detected tissue and filtered out all artifacts, white space, and non-tissue pixels. The second algorithm detected red (+) stained tissue versus non-stained tissue regions, and in the third and final step, the ratio of the area occupied by the red (+) pixels were normalized to the total tissue area.

### Statistics

Prism 8 (GraphPad Software) was used for all the statistical analyses. IC<sub>50</sub> and IC<sub>80</sub> for the reporter and whole blood assays were calculated based on the nonlinear regression. Least square means (LS means) and their 95% confidence intervals (CIs) were estimated after log<sub>10</sub> transformation in a mixed effect model with subject as a random effect. The LS means and their CIs were then transformed back to the original scale for reporting purpose. The LS means of IC<sub>50</sub> or IC<sub>80</sub> for the risankizumab-treated group were head-to-head compared with those of each individual antibody treated group. The *p*-values were generated from Student *t*-test and the Tukey HSD test after adjusting for multiple comparisons.

All in vivo studies have been repeated and confirmed. Data were analyzed using one-way and two-way ANOVAs followed by Tukey's and Sidak's multiple comparison post hoc analyses, respectively, if the ANOVA revealed significance. A *p*-value less than 0.05 was considered significant.

### Study approval

Human whole blood samples were acquired from healthy donors under an AbbVie Institutional Review Board-approved protocol. Cord blood samples were provided by LifeSouth Community Blood Centers under Blood Center Board of Directors approved the protocol. The appropriate written informed consent was obtained from all the donors prior to the studies. The studies were performed in adherence to the Declaration of Helsinki Principles.

### Acknowledgments

The authors would like to thank the following AbbVie colleagues: Debra Touw, Limary Medina, Sahana Bose, Joel Cohen-Solal, Meha Chhaya, Daniel Serna, Liang Zhang, Soumya Mitra, Munish Puri, and Stephanie Paulsboe for technical contributions, James Fann and Jie Cheng for statistical support and Eric Goedken for scientific discussions. This work was funded by AbbVie Inc. AbbVie participated in the study design, research, data collection, analysis, interpretation of data, writing, reviewing, and approving the publication.

### Disclosure statement

Mark Konrad, Denise Perron, Yibing Wang, Jun Zhang and Gary Overmeyer are former AbbVie employees and may own AbbVie stock. All other listed authors are AbbVie employees and may own AbbVie stock.

### ORCID

Li Zhou  <http://orcid.org/0000-0002-9683-3562>

### Data availability

The data that support the findings of this study are available from the authors on reasonable request; see author contributions for specific data sets.

### Abbreviations

CyToF	cytometry by time of flight
DSC	differential scanning calorimetry
FACS	fluorescence-activated cell sorting
HDX-MS	hydrogen deuterium exchange mass spectrometry
i.p.	intraperitoneally
IHC	immunohistochemistry
ITC	isothermal titration calorimetry
$k_a$	association rate constant
$k_d$	dissociation rate constant
$K_D$	equilibrium dissociation constant
nanoDSF	nano differential scanning fluorimetry
Sc	single-chain
SPR	surface plasmon resonance
$T_{agg}$	temperature of protein aggregation
$T_{H17}$	T helper 17
UMAP	uniform manifold approximation and projection.

### References

1. Website International Federation of Psoriasis Associations (IFPA) Our Cause: Psoriasis. [Accessed 03]. <https://ifpa-psy.com/our-cause>

2. Chiricozzi A, Romanelli P, Volpe E, Borsellino G, Romanelli M. Scanning the Immunopathogenesis of Psoriasis. *Int J Mol Sci*. 2018;19(1):1. doi:10.3390/ijms19010179.
3. Di Cesare A, Di Meglio P, Nestle FO. The IL-23/Th17 axis in the immunopathogenesis of psoriasis. *J Invest Dermatol*. 2009;129(6):1339–50. doi:10.1038/jid.2009.59.
4. Chiricozzi A, Saraceno R, Chimenti MS, Guttman-Yassky E, Krueger JG. Role of IL-23 in the pathogenesis of psoriasis: a novel potential therapeutic target? *Expert Opin Ther Targets*. 2014;18(5):513–25. doi:10.1517/14728222.2014.889686.
5. Benson JM, Peritt D, Scallon BJ, Heavner GA, Shealy DJ, Giles-Komar JM, Mascelli MA. Discovery and mechanism of ustekinumab: a human monoclonal antibody targeting interleukin-12 and interleukin-23 for treatment of immune-mediated disorders. *MAbs*. 2011;3(6):535–45. doi:10.4161/mabs.3.6.17815.
6. Benson JM, Sachs CW, Treacy G, Zhou H, Pendley CE, Brodmerkel CM, Shankar G, Mascelli MA. Therapeutic targeting of the IL-12/23 pathways: generation and characterization of ustekinumab. *Nat Biotechnol*. 2011;29(7):615–24. doi:10.1038/nbt.1903.
7. Benson J, Carton J, Cunningham M, Orlovsky Yevgeniya I, Rauchenberger R, Sweet R Human anti-il-23 antibodies, compositions, methods and uses. US 9353181 B2, 2012/06/15, 2016.
8. Kopp T, Riedl E, Bangert C, Bowman EP, Greisenegger E, Horowitz A, Kittler H, Blumenschein WM, McClanahan TK, Marbury T, et al. Clinical improvement in psoriasis with specific targeting of interleukin-23. *Nature*. 2015;521(7551):222–26. doi:10.1038/nature14175.
9. Singh S, Kroe-Barrett RR, Canada KA, Zhu X, Sepulveda E, Wu H, He Y, Raymond EL, Ahlberg J, Frego LE, et al. Selective targeting of the IL23 pathway: generation and characterization of a novel high-affinity humanized anti-IL23A antibody. *MAbs*. 2015;7(4):778–91. doi:10.1080/19420862.2015.1032491.
10. Gordon KB, Duffin KC, Bissonnette R, Prinz JC, Wasfi Y, Li S, Shen YK, Szapary P, Randazzo B, Reich K. A phase 2 trial of guselkumab versus adalimumab for plaque psoriasis. *N Engl J Med*. 2015;373(2):136–44. doi:10.1056/NEJMoa1501646.
11. Blauvelt A, Papp KA, Griffiths CE, Randazzo B, Wasfi Y, Shen YK, Li S, Kimball AB. Efficacy and safety of guselkumab, an anti-interleukin-23 monoclonal antibody, compared with adalimumab for the continuous treatment of patients with moderate to severe psoriasis: results from the phase III, double-blinded, placebo- and active comparator-controlled VOYAGE 1 trial. *J Am Acad Dermatol*. 2017;76:405–17.
12. Reich K, Armstrong AW, Foley P, Song M, Wasfi Y, Randazzo B, Li S, Shen YK, Gordon KB. Efficacy and safety of guselkumab, an anti-interleukin-23 monoclonal antibody, compared with adalimumab for the treatment of patients with moderate to severe psoriasis with randomized withdrawal and retreatment: results from the phase III, double-blind, placebo- and active comparator-controlled VOYAGE 2 trial. *J Am Acad Dermatol*. 2017;76:418–31.
13. Reich K, Papp KA, Blauvelt A, Tying SK, Sinclair R, Thaci D, Nograles K, Mehta A, Cichanowitz N, Li Q, et al. Tildrakizumab versus placebo or etanercept for chronic plaque psoriasis (reSURFACE 1 and reSURFACE 2): results from two randomised controlled, phase 3 trials. *Lancet*. 2017;390(10091):276–88. doi:10.1016/S0140-6736(17)31279-5.
14. Papp KA, Blauvelt A, Bukhalo M, Gooderham M, Krueger JG, Lacour J-P, Menter A, Philipp S, Sofen H, Tying S, et al. Risankizumab versus ustekinumab for moderate-to-severe plaque psoriasis. *N Engl J Med*. 2017;376(16):1551–60. doi:10.1056/NEJMoa1607017.
15. Gordon KB, Strober B, Lebwohl M, Augustin M, Blauvelt A, Poulin Y, Papp KA, Sofen H, Puig L, Foley P, et al. Efficacy and safety of risankizumab in moderate-to-severe plaque psoriasis (UltIMMa-1 and UltIMMa-2): results from two double-blind, randomised, placebo-controlled and ustekinumab-controlled phase 3 trials. *Lancet*. 2018;392(10148):650–61. doi:10.1016/S0140-6736(18)31713-6.
16. McKeage K, Duggan S. Risankizumab: first global approval. *Drugs*. 2019;79(8):893–900. doi:10.1007/s40265-019-01136-7.
17. Reich K, Gooderham M, Thaci D, Crowley JJ, Ryan C, Krueger JG, Tsai T-F, Flack M, Gu Y, Williams DA, et al. Risankizumab compared with adalimumab in patients with moderate-to-severe plaque psoriasis (IMMvent): a randomised, double-blind, active-comparator-controlled phase 3 trial. *The Lancet*. 2019;394(10198):576–86. doi:10.1016/S0140-6736(19)30952-3.
18. Leonard CL, Kimball AB, Papp KA, Yeilding N, Guzzo C, Wang Y, Li S, Dooley LT, Gordon KB, Investigators PS. Efficacy and safety of ustekinumab, a human interleukin-12/23 monoclonal antibody, in patients with psoriasis: 76-week results from a randomised, double-blind, placebo-controlled trial (PHOENIX 1). *Lancet*. 2008;371(9625):1665–74. doi:10.1016/S0140-6736(08)60725-4.
19. Papp KA, Langley RG, Lebwohl M, Krueger GG, Szapary P, Yeilding N, Guzzo C, Hsu M-C, Wang Y, Li S, et al. Efficacy and safety of ustekinumab, a human interleukin-12/23 monoclonal antibody, in patients with psoriasis: 52-week results from a randomised, double-blind, placebo-controlled trial (PHOENIX 2). *Lancet*. 2008;371(9625):1675–84. doi:10.1016/S0140-6736(08)60726-6.
20. Koutruba N, Emer J, Lebwohl M. Review of ustekinumab, an interleukin-12 and interleukin-23 inhibitor used for the treatment of plaque psoriasis. *Ther Clin Risk Manag*. 2010;6:123–41.
21. Nakamura M, Lee K, Jeon C, Sekhon S, Afifi L, Yan D, Lee K, Bhutani T. Guselkumab for the treatment of psoriasis: a review of phase III trials. *Dermatol Ther (Heidelb)*. 2017;7(3):281–92. doi:10.1007/s13555-017-0187-0.
22. Yao Z, Hu C, Zhu Y, Xu Z, Randazzo B, Wasfi Y, Chen Y, Sharma A, Zhou H. Population pharmacokinetic modeling of guselkumab, a human IgG1lambda monoclonal antibody targeting IL-23, in patients with moderate to severe plaque psoriasis. *J Clin Pharmacol*. 2018;58(5):613–27. doi:10.1002/jcph.1063.
23. Khalilieh S, Hodsman P, Xu C, Tzontcheva A, Glasgow S, Montgomery D. Pharmacokinetics of Tildrakizumab (MK-3222), an anti-IL-23 monoclonal antibody, after intravenous or subcutaneous administration in healthy subjects. *Basic Clin Pharmacol Toxicol*. 2018;123(3):294–300. doi:10.1111/bcpt.13001.
24. Suleiman AA, Minocha M, Khatri A, Pang Y, Othman AA. Population pharmacokinetics of risankizumab in healthy volunteers and subjects with moderate to severe plaque psoriasis: integrated analyses of phase I-III clinical trials. *Clin Pharmacokinet*. 2019;58, 1309–1321.
25. Roopenian DC, Akilesh S. FcRn: the neonatal Fc receptor comes of age. *Nat Rev Immunol*. 2007;7(9):715–25. doi:10.1038/nri2155.
26. Romagnani S, Maggi E, Liotta F, Cosmi F, Annunziato F. Properties and origin of human Th17 cells. *Mol Immunol*. 2009;47(1):3–7. doi:10.1016/j.molimm.2008.12.019.
27. Billerbeck E, Kang Y-H, Walker L, Lockstone H, Grafmueller S, Fleming V, Flint J, Willberg CB, Bengsch B, Seigel B, et al. Analysis of CD161 expression on human CD8+ T cells defines a distinct functional subset with tissue-homing properties. *Proc Natl Acad Sci U S A*. 2010;107(7):3006–11. doi:10.1073/pnas.0914839107.
28. Presta Leonard G Engineered Anti-il-23p19 Antibodies. US 8293883 B2, 2008/02/21, 2012.
29. Bloch Y, Bouchareychas L, Merceron R, Skladanowska K, Van den Bossche L, Detry S, Govindarajan S, Elewaut D, Haerynck F, Dullaers M, et al. Structural activation of pro-inflammatory human cytokine IL-23 by cognate IL-23 receptor enables recruitment of the shared receptor IL-12Rβ1. *Immunity*. 2018;48(1):45–58 e6. doi:10.1016/j.immuni.2017.12.008.
30. Luo J, Wu SJ, Lacy ER, Orlovsky Y, Baker A, Teplyakov A, Obmolova G, Heavner GA, Richter HT, Benson J. Structural basis for the dual recognition of IL-12 and IL-23 by ustekinumab. *J Mol Biol*. 2010;402(5):797–812. doi:10.1016/j.jmb.2010.07.046.

31. Manel N, Unutmaz D, Littman DR. The differentiation of human T(H)-17 cells requires transforming growth factor-beta and induction of the nuclear receptor RORgamma. *Nat Immunol.* 2008;9(6):641–49. doi:10.1038/ni.1610.
32. McGeachy MJ, Chen Y, Tato CM, Laurence A, Joyce-Shaikh B, Blumenschein WM, McClanahan TK, O'Shea JJ, Cua DJ. The interleukin 23 receptor is essential for the terminal differentiation of interleukin 17-producing effector T helper cells in vivo. *Nat Immunol.* 2009;10(3):314–24. doi:10.1038/ni.1698.
33. Lee Y, Awasthi A, Yosef N, Quintana FJ, Xiao S, Peters A, Wu C, Kleinewietfeld M, Kunder S, Hafler DA, et al. Induction and molecular signature of pathogenic TH17 cells. *Nat Immunol.* 2012;13(10):991–99. doi:10.1038/ni.2416.
34. Gauld SB, Gauvin D, Olson L, Leys L, Paulsboe S, Liu Z, Edelmayer RM, Wetter J, Salte K, Wang Y, et al. Mechanistic and pharmacological assessment of murine IL-23 mediated psoriasis-form dermatitis; implications for drug discovery. *J Dermatol Sci.* 2018;92(1):45–53. doi:10.1016/j.jdermsci.2018.08.001.
35. Wang Y, Edelmayer R, Wetter J, Salte K, Gauvin D, Leys L, Paulsboe S, Su Z, Weinberg I, Namovic M, et al. Monocytes/Macrophages play a pathogenic role in IL-23 mediated psoriasis-like skin inflammation. *Sci Rep.* 2019;9(1):5310. doi:10.1038/s41598-019-41655-7.
36. Suarez-Farinas M, Arbeit R, Jiang W, Ortenzio FS, Sullivan T, Krueger JG, Fang D. Suppression of molecular inflammatory pathways by Toll-like receptor 7, 8, and 9 antagonists in a model of IL-23-induced skin inflammation. *PLoS One.* 2013;8(12):e84634. doi:10.1371/journal.pone.0084634.
37. Hoeve MA, Savage ND, De Boer T, Langenberg DM, de Waal Malefyt R, Ottenhoff TH, Verreck FA. Divergent effects of IL-12 and IL-23 on the production of IL-17 by human T cells. *Eur J Immunol.* 2006;36(3):661–70. doi:10.1002/eji.200535239.
38. Wang X, Wei Y, Xiao H, Liu X, Zhang Y, Han G, Chen G, Hou C, Ma N, Shen B, et al. A novel IL-23p19/Ebi3 (IL-39) cytokine mediates inflammation in Lupus-like mice. *Eur J Immunol.* 2016;46(6):1343–50. doi:10.1002/eji.201546095.
39. Bridgewood C, Alase A, Watad A, Wittmann M, Cuthbert R, McGonagle D. The IL-23p19/EBI3 heterodimeric cytokine termed IL-39 remains a theoretical cytokine in man. *Inflamm Res.* 2019;68(6):423–26. doi:10.1007/s00011-019-01235-x.
40. Ramnath D, Tunny K, Hohenhaus DM, Pitts CM, Bergot AS, Hogarth PM, Hamilton JA, Kapetanovic R, Sturm RA, Scholz GM, et al. TLR3 drives IRF6-dependent IL-23p19 expression and p19/EBI3 heterodimer formation in keratinocytes. *Immunol Cell Biol.* 2015;93(9):771–79. doi:10.1038/icb.2015.77.
41. Tabrizi MA, Klakamp SL. Considerations for construct and affinity design goals. In: Tabrizi MA, Bornstein GG, Klakamp SL, editors. *Development of antibody-based therapeutics: translational considerations & challenges.* Adis, Singapore: Springer Singapore; 2018. p. 19–40.
42. Presky DH, Minetti LJ, Gillessen S, Wilkinson VL, Wu CY, Gubler U, Chizzonite R, Gately MK. Analysis of the multiple interactions between IL-12 and the high affinity IL-12 receptor complex. *J Immunol.* 1998;160:2174–79.
43. Presta Leonard G Engineered Anti-il-23r Antibodies. WO 2008/106134 A2, 2008/02/26, 2008.
44. Stockmann H, Todorovic V, Richardson PL, Marin V, Scott V, Gerstein C, Lake M, Wang L, Sadhukhan R, Vasudevan A. Cell-surface receptor–ligand interaction analysis with homogeneous time-resolved FRET and metabolic glycan engineering: application to transmembrane and gpi-anchored receptors. *J Am Chem Soc.* 2017;139(46):16822–29. doi:10.1021/jacs.7b09359.
45. Zhou L, Zhang J, DiGiammarino E, Kavishwar A, Yan B, Chumsae C, Ihnat PM, Powers D, Harlan J, Stine WB. PULSE SPR: a high throughput method to evaluate the domain stability of antibodies. *Anal Chem.* 2018;90(20):12221–29. doi:10.1021/acs.analchem.8b03452.
46. Schlothauer T, Rueger P, Stracke JO, Hertenberger H, Fingas F, Kling L, Emrich T, Drabner G, Seeber S, Auer J, et al. Analytical FcRn affinity chromatography for functional characterization of monoclonal antibodies. *MAbs.* 2013;5(4):576–86. doi:10.4161/mabs.24981.